JMEPEG
https://doi.org/10.1007/s11665-023-08960-9

1059-9495/$19.00

ORIGINAL RESEARCH ARTICLE

Unraveling Electrochemical Mechanisms in Plasma Electrolytic Oxidation of Cold Spray Additively Manufactured Stainless Steel

Alessandro M. Ralls, Robert Gillespy, Pramod V. Menezes, and Pradeep L. Menezes

Submitted: 1 July 2023 / Revised: 4 October 2023 / Accepted: 28 October 2023

Cold spray additive manufacturing (CSAM) has gained significant attention for its rapid solid deposition capabilities. However, the presence of defects such as pores and voids limits its performance, particularly in electrochemical environments. In this study, a novel post-surface treatment, plasma electrolytic oxidation (PEO), was applied and investigated as a feasible solution to overcome these defects. Results demonstrated a successful PEO deposition on cold-sprayed 316L stainless steel (SS) due to the rapid formation and discharge of aluminate electrolytes along the surface. However, due to the severely strained and highly crystalline surface, the electric field that allows for the deposition of $Al(OH)^{4-}$ anions was reduced. As consequence, an uneven and rough deposition took place. Nonetheless, a successful Al_2O_3 film of 12.30 μm thickness was formed. Experimental tests were further conducted in simulated aqueous and biological-based solutions to test the electrochemical resistance of the deposit. Results reveal a noticeable enhancement in corrosion resistance for both solutions. This enhancement can be attributed to the "postponing" and "blocking" effect enabled by the Al_2O_3 film, which prevented the electrolyte solution from penetrating the CS surface. Collectively, these findings suggest that PEO is indeed a promising technique to mitigate the chemical degradation of CSAM'd 316L SS.

Keywords cold spray, corrosion, pitting, plasma electrolytic oxidation, steel, surface modification

1. Introduction

In recent years, there has been a great attraction toward the industrial application of cold spray additive manufacturing (CSAM), more commonly referred to as cold spray (CS). Relative to fusion-based additive manufacturing (AM) techniques [e.g., powder bed fusion (PBF), wire-fed fusion (WFF), and thermal spraying (TS) (Ref 1-3)], the CS process is truly unique as the deposition process solely relies on the plastic deformation of rapidly accelerated particles (most commonly found within the range of 5 and 50 μm) rather than fusion of particle/wired materials through a thermal source (Ref 4-6). To conceptualize the CS process, powders are first fed through a feedstock source into a De-Laval (convergent-divergent). Upon entry, a high-pressure gas (of either N_2 and/or He composition) expands and rapidly accelerates the particles to supersonic speeds, typically varying from 500 to 1500 m/s (Ref 7). Upon collision, the particles will mechanically and physiochemically bond due to the combination of high strain rates and severe plastic deformation. Over time, these particles continually build up thus resulting in dense and high-quality deposits (Ref 8-10).

Among the variety of materials used, stainless steel (SS) has been increasingly utilized due to its excellent resistance to electrochemical degradation. This advantage is particularly attributed to the sufficient quantities of chromium (Cr) and nickel (Ni) within its elemental structure. Especially with γ and γ/α dominant structures, the Cr content allows for the formation of a protective Cr_2O_3 film (typically of 1-3 nm thickness), while the Ni content helps maintain the film (Ref 11-13). From a microstructural standpoint, the high-density grain boundaries of the severely work-hardened surface also allow for quicker Cr diffusion rates, thus resulting in quicker overall film conduction (Ref 14, 15). This can especially be seen in the 316L grade of SS, in which many have successfully fabricated robust, corrosion-resistant deposits. From an industrial standpoint, CS deposits can be used in a plethora of applications in corrosion-based environments, such as in the marine, nuclear, and biomedical-based sectors (Ref 16, 17). In combination with the rapid and ease of deposition associated with the CS process, this additive technology has great industrial relevance.

However, despite these advantages, a common defect seen in CS-based 316L SS deposits is the presence of porosity and voids. These unavoidable defects are attributed to the lack of uniform particle deformation upon impact, as the feedstock powder for all CS-deposited materials will always have some size/geometrical variation (Ref 18). These defects can be quite detrimental, as the instability of the passive film due to the porous surface can result in unwanted pitting and exacerbated corrosion rates. This was seen in our earlier work with CSAM 316L (Ref 19), in which we found that despite the extremely refined microstructure of the deposit, the porous surface defects

Alessandro M. Ralls, Robert Gillespy, and **Pradeep L. Menezes**, Department of Mechanical Engineering, University of Nevada, Reno, Nevada 89557; and **Pramod V. Menezes**, Institute of Electrochemistry, Ulm University, Albert-Einstein-Allee 47, 89081 Ulm, Germany. Contact e-mail: pmenezes@unr.edu.

Published online: 27 November 2023

resulted in greater pit formations and similar corrosion rates compared to traditionally casted 316L SS. As such, there is an increasing need to improve the surface quality of these deposits to improve their electrochemical performances.

To overcome these defects, post-processing techniques are most frequently used to improve their structural integrity. One of the most commonly used techniques used is heat treatment (HT). By effectively inducing atomic diffusion, the porosity is effectively recrystallized into a denser structure. However, due to the softening and grain growth-like effects induced by HT, the corrosion resistance is further diminished (Ref 14). Other deformation techniques such as friction stir processing (FSP) can also be used (Ref 20). However, performing this treatment will require a complex setup and, in some cases, will require pre-processing HT to reduce the likelihood of brittle fracture upon processing. Similarly, a thermal–mechanical affected zone (TMAZ) will also exist, which can result in uneven stresses along the surface. Moreover, other deformation-focused technologies can roughen the surface, which can be detrimental to corrosion resistance.

Comparatively, one technology that combats both of these drawbacks is plasma electrolytic oxidation (PEO) (Ref 21). In essence, PEO is a plasma-assisted electrochemical technique that allows for the synthesis of a protective ceramic-oxide layer (typically within the range of 1-100 μm) along a material's surface (Ref 22, 23). Mechanistically, the fundamental premise for PEO lies in the plasma discharge phenomenon that occurs when voltage is applied. At a certain point, the existing oxide layer on the working substrate will break down, thus allowing for the formation of a crystalline oxide layer (Ref 24). In recent years, the feasibility, understanding, and application of PEO technology have significantly grown. For example, for niobium materials, the application of PEO has recently been reported to improve the osseointegration of biomedical implants due to the formation of surface features such as topography and porosity (Ref 25). Other bio-based materials such as zirconium, zinc, and titanium have also been proposed as ideal candidates for PEO treatment, as the outer and barrier ceramic layers (formed from aluminate, silicate, phosphate, and calcium-based electrolytes) improve electrochemical resistance (Ref 26-28). For materials such as magnesium, dual PEO layering has been additionally studied using materials such as polymers to cover surface cracking and porosity (Ref 29, 30). Even in semiconductor photocatalytic applications, the formation of photoactive TiO_2 phases (from Ti-based substrates) during PEO has greatly been investigated (Ref 31, 32).

Among all these materials, they all share a key theme. This theme is tied into the valve metal characteristics that they have, as their electrochemical characteristics allow for the formation of anodic charges along the surface, which result in a thick protective coating (Ref 22, 33, 34). However, on the flip side, with non-valve metals such as SS, these critical discharges cannot occur, thus presenting a problem for proper PEO deposition (Ref 35). This can largely be due to the kinetically unfavorable process that valve metals have during the oxidation process (Ref 36). With an increasing amount of research in the field, a few have been able to successfully deposit Al_2O_3 layers due to the decomposition of aluminate electrolytes during deposition (Ref 37, 38). This dissolution allows for the formation of a barrier similar to what's seen with valve metals, thus allowing for a protective layer for corrosion resistance.

To date, there is limited knowledge pertaining to the mechanisms and performance of PEO-deposited films on 316L SS materials. In the case of CS 316L SS, there are no existing works that have studied the feasibility of PEO deposition, let alone its electrochemical properties. As such, the objective of this work is to provide a novel understanding of the feasibility of PEO deposition on CS 316L SS substrates. In addition, we also aim to study the electrochemical characteristics of this newly formed layer and understand how it can be used to improve the CS coating's corrosion resistance. Being the first article to focus on the deposition of PEO for a non-valve metal formed from CS, the intention of this work is to provide new insight into the possibilities of PEO for non-valve metals and to understand how it can be used to improve their corrosion resistance. By doing so, we hope to form a new direction in which the future of the field can grow.

2. Materials and Methods

2.1 Materials

The feedstock powder used in this research consisted of a gas-atomized commercially pure (CP) 316L SS powder obtained from Sigma-Aldrich (St. Louis, MO, USA). The powder's elemental composition consisted of Fe-18Cr-10Ni-3Mo. This powder was then sprayed as a freestanding deposit using a state-of-the-art high-pressure CS system (Impact Innovation GmbH, Rattenkirchen, Germany). For reference, the corresponding spraying parameters can be seen in Table 1. The average variation in powder morphology and diameter distribution was calculated to be 20.17 μm size with a standard deviation of 6.64 μm. It can be noted that there exist some variations in the powder morphology, largely in the forms of particle satellites and non-spherical geometries, as shown in Fig. 1. Due to the nature of the gas-atomization process, it is to be expected that some variation in particle morphology exists. Consequentially, due to the non-even distribution of particle plastic deformation upon impact, the aforementioned formation of pores and voids can occur.

2.2 PEO Deposition

Prior to PEO treatment, the deposited CS specimens were sectioned into the dimensions of $\sim 1 \times 1$ cm^2. Each sample was then polished using successive grades of sandpaper up to a grit size of 1200, which resulted in an average surface roughness (S_a) of 0.2 ± 0.05 μm. Following polishing, each sample was carefully washed and ultra-sonicated in ethanol for a total of 20 min and dried using a stream of warm air. Afterward, each PEO experiment was conducted in a double-walled glass cell (Fig. 2). The setup essentially consisted of a simple asymmetric two-electrode system, which consisted of the CS steel of a 0.43 cm^2 working surface being the anode and a wrought 316L SS plate cathode of $20 \times 20 \times 2$ mm^3 dimensions being a cathode. Understanding that 316L SS is not a valve metal, to ensure the formation of the PEO coating, a barrier layer of Al_2O_3 was deposited using an aluminate-based electrolyte solution composed of 0.05 M NaOH + 0.05 M $NaAl_2O_3$ in a DI-water solution (Ref 35). To perform oxidation, a DC power supply source (TDK-Lambda Programmable, GEN600-1.3/E, 1U, 780W, RS-232/RS-485) was utilized. The current was set constant at 3 A, with variations in the voltage from 0-700 V for a total of 1 min. To control the heating of the electrolyte during deposition, water cooling through the double-

Table 1 The high-pressure CS processing parameters used for this work

Propellant gas	Sprayed material	Gas temperature, °C	Gas pressure, MPa	Spray angle, angle, degree	Stand-off distance, mm	Step size, mm	Powder feed rate, RPM	Powder carrier gas flow rate, m^3/h	Nozzle type
N_2	316L	850-1100	4.0-5.0	90°	25.4	0.762	2.0-3.0	3.0-4.0	SiC water-cooled nozzle

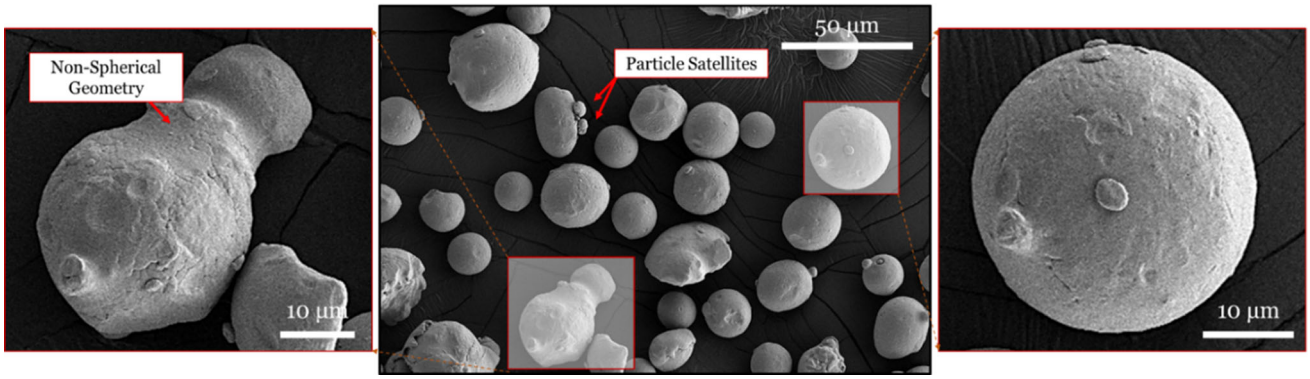

Fig. 1 The morphology of the gas-atomized 316L SS feedstock powder

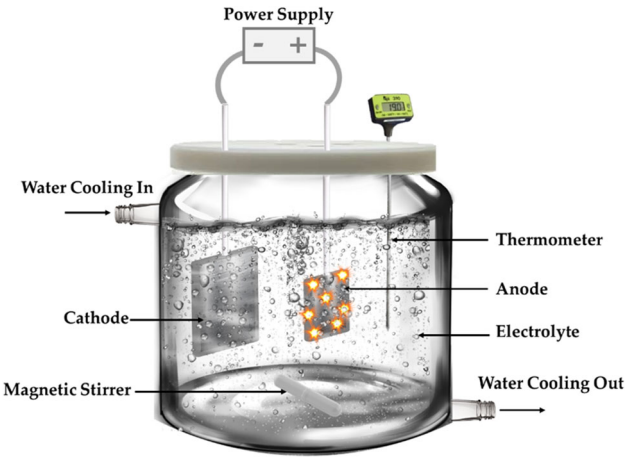

Fig. 2 A visualization of the double-walled glass cell and experimental setup used for PEO deposition

walled glass cell was employed, of which the electrolyte temperature remained between 30 °C and 40 °C. Additionally, the electrolyte was magnetically stirred during the deposition process to ensure that no concentration gradients occurred (Ref 39). Post-experimentation, each specimen was carefully rinsed with deionized water. For reference, the PEO CS specimen will be referred to as CS + PEO.

2.3 Characterization Techniques

Pre- and post-deposition, the surface morphology of the CS substrates was characterized using a Rtec 3D profilometer attached to a Rtec-Tribometer (Rtec-Instruments, San Jose, CA, USA) containing a resolution of 50 nm. A scanning area of 2×1 mm^2 was applied to quantify the changes in surface roughness parameters associated with the deposition. These changes were quantified using the open-source Gwyddion software (Ref 40). The surface was characterized using optical and scanning electron microscopy (SEM) imaging, whereas the cross section was characterized using field emission scanning electron microscopy (FESEM). For optical imaging, a fluorescence microscope (Zeiss, White Plains, NY) was utilized. For surface SEM imaging, JSM-6010LA InTouchScope SEM (JEOL, Tokyo Japan) was employed using a secondary electron (SE) mode. For cross-sectional FESEM imaging, a JSM-7100FR FESEM (JEOL, Tokyo Japan) was used. To examine the cross section, the PEO substrate was first carefully sectioned and abraded with the same method mentioned in Section 2.2. The cross section was then gently polished using 3 and 1 μm diamond pastes, with subsequent ultrasonication in ethanol. Afterward, a conductive carbon coating was sputtered, which helped to minimize distortion and charging from the Al_2O_3 coating. To further validate that deposition of the PEO coating took place, elemental analysis of the surface was taken using energy-dispersive x-ray spectroscopy (EDS). Additionally, a Bruker-D2 Phase (Bruker, Madison, WI, USA) x-ray diffractometer (XRD) with Cu-Kα radiation was utilized to validate any change in phase composition. The accelerating voltage was set to 40 kV with a corresponding current of 30 mA. The scanning speed was set at 1°/min with a step size of 0.02° across a scan range of 20° to 100°.

2.4 Electrochemical Testing

To study the electrochemical characteristics of the pre- and post-PEO deposited substrates, potentiodynamic polarization (PDP) experiments were conducted as per ASTM G597-97 (Ref 41). All electrochemical tests were conducted at an ambient room temperature of $\sim$ 25 °C using a two-electrolytic solution. The first solution consisted of a naturally aerated 3.5 wt.% NaCl (mass fraction) solution, whereas the second consisted of a commercially available Hanks' balanced salt

solution (HBSS, Quality Biological Inc., MD, USA). In the case of the HBSS solution, a composition consisting of 0.400 g/L KCl, 0.060 g/L KH_2PO_4, 8.000 g/L NaCl, 0.350 g/L $NaHCO_3$, 0.048 g/L Na_2HPO_4 (anhydrous), and 1 g/L D-Glucose was utilized. Each series of tests were conducted using a Gamry Reference 3000 potentiostat (Gamry Instruments, Warminster, PA, USA) using a three-electrode configuration. The CS specimen (both pre- and post-PEO treatment) was set as the working electrode having the same exposed area (0.43 cm^2) as the initial PEO treatment. A graphite block was used as the counter-electrode with the reference electrode consisting of a saturated calomel electrode (SCE). Prior to experimentation, the working surface of each sample was cleaned using the same methods mentioned in Section 2.2. To ensure that all samples were in electrochemical equilibrium, open circuit potential (OCP) tests were conducted for a total of 3600 s. After OCP testing, PDP scans were employed at 1000 mV below the OCP stabilization, of which a scan range of 1 mV s^{-1} was applied until the voltage reached 1000 mV above the OCP point. Post-experimentation, the current density was determined by taking the slopes of the anodic and cathodic currents of the Tafel curve and finding the value in which they intersect at the equilibrium corrosion potential (Ref 42). The corroded surfaces were then characterized using the same profilometer/optical/SEM devices mentioned in Section 2.3. To better understand the change in corrosion resistance, electrochemical impedance spectroscopy (EIS) experiments were also conducted. The AC signal was set to 10 mV with the working frequency range varying from 100 KHz to 10 mHz. To ensure repeatability, each test was performed a total of three times.

3. Results

3.1 *j–U* Characteristics

In order to optimize the electrolysis process, stationary current density–voltage (*j–U*) curves of the CS specimen in freshly prepared electrolytic solutions were obtained. To conduct such tests, a wide array of voltages spanning from 300, 400, 500, 600, and 700 V were applied. The results of these findings can be seen in Fig. 3 alongside their corresponding optical graphs during electrolysis. There are a few key observations that can be taken away from these findings. First, it can be noted that the *j–U* characteristics of the CS specimen can be broken into three key stages. In the first stage (Stage A), there was a gradual increase in the current density as a function of voltage. Interestingly enough, evidence of a gaseous envelope began to take place at the 300 V range, which indicates that there is some decomposition of aluminate electrolytes nearby the working electrode (i.e., CS) surface (Ref 39). As the voltage gradually increases, the oxide layer along the CS surface is effectively broken down with micro-discharging gradually increasing (Ref 43). Out of the tested voltages, the greatest amount of visual microplasma was at 400 V (Stage B). After 400 V, an orange-like spark begins to form along the surface. The intensity of this colored spark begins to visually drastically increase as voltage increases (Stage C). In some cases, a large amount of plasma formed will result in extreme plasma heat, which can be detrimental to PEO deposition (Ref 44). Nonetheless, it can be noted that despite this formation, there is no evidence of a "breakdown potential," as the current density appears to gradually increase. This finding suggests that a higher degree of plasma activity is occurring along the surface. Likely, the occurrence of non-uniform plasma discharging is attributed to this finding. Nonetheless, after visual inspection of each specimen post-PEO, it was determined that the PEO sample formed at 400 V had the greatest deposition. As such, the remainder of this work will solely focus on this specifically optimized parameter.

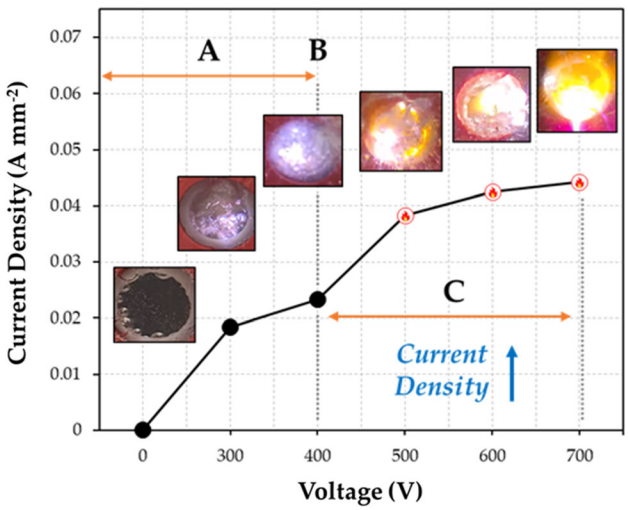

Fig. 3 The current density vs. voltage plots of the electrolysis for CS 316L SS in 0.05 M NaOH + 0.05 M $NaAl_2O_3$ solution

3.2 Surface Characterization

To understand the formation of the PEO film along the CS substrate surface, the surface morphologies of the CS and CS + PEO substrates were investigated. As shown in Fig. 4, there is a stark difference between the surface features from both three-dimensional (3D) and two-dimensional (2D) perspectives. Pre-PEO, the surface features of the CS specimen (Fig. 4a and b) are of a typical grounded texture. As evident by the 2D profile (Fig. 4c), the surface roughness is slightly varied, with some evidence of small pores along the surface. Such defects are to be expected from the CS process. However, upon PEO deposition, the CS + PEO sample exhibited a much different morphology (Fig. 4d). Although evidence of Al_2O_3 deposition is shown from the white regions along the exposed surface, its thickness and evenness in distribution are quite varied. Upon closer inspection, these observations are further confirmed through 3D/2D profile measurements (Fig. 4e and f), as the surface appeared to be roughened. These findings are not uncommon, as variations in the bubble formation of the treatment process can result in uneven current transfers through the sample surface (Ref 45). Given the trend of the *j–U* plots, it is likely that the hydrogen bubble formation affected the evenness of the film. However, to further validate these observations, surface roughness measurements were quantified in the forms of S_a, root-mean-square height (S_q), skewness (S_{sk}), and kurtosis (S_{ku}). These findings are listed in Table 2. In the case of S_a and S_q, the surface roughness increased by 19.5% and 30.2%, thus validating the visual observations. Similarly, it was observed that S_{sk} and S_{ku} increased by 140.0% and 75.15%. Typically, when S_{ku} increases, the surface begins to exhibit a leptokurtic type of distribution. This finding indicates that high peaks and low valleys exist along the surface, which

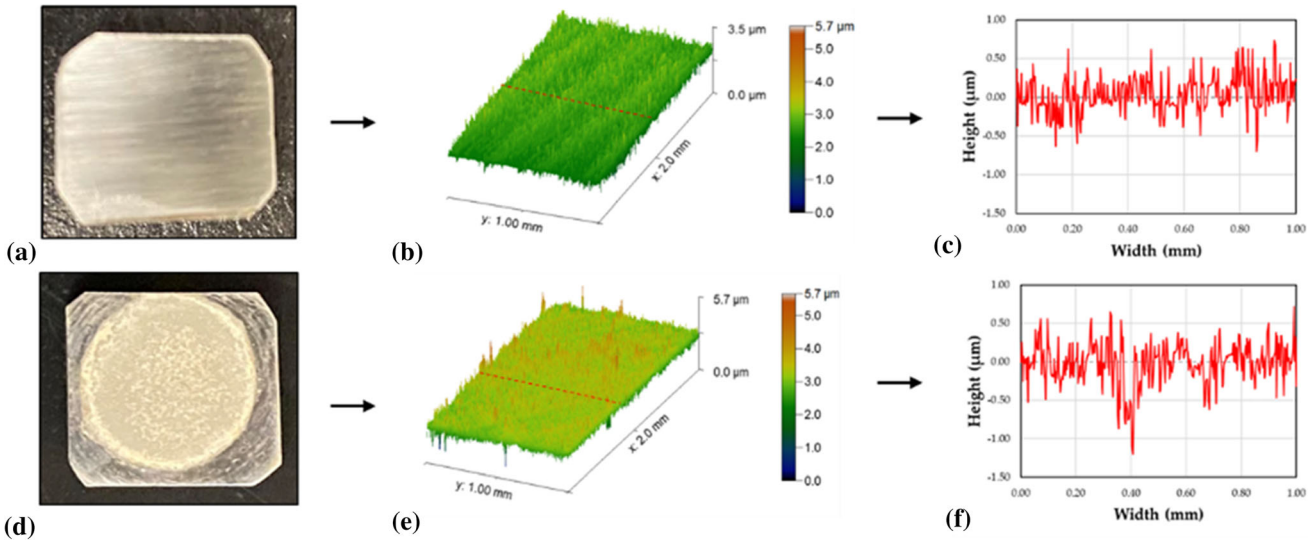

Fig. 4 The change in surface morphology of the (a-c) CS and (d-f) CS + PEO substrates

Table 2 The change in surface roughness characteristics for the CS and CS + PEO substrates

	S_q, nm	S_a, nm	S_{sk}	S_{ku}
CS	228.5	185.5	0.029	1.31
CS + PEO	297.6	221.8	0.069	2.30
CS → CS + PEO Δ	+ 30.2%	+ 19.5%	+ 140.0%	+ 75.15%

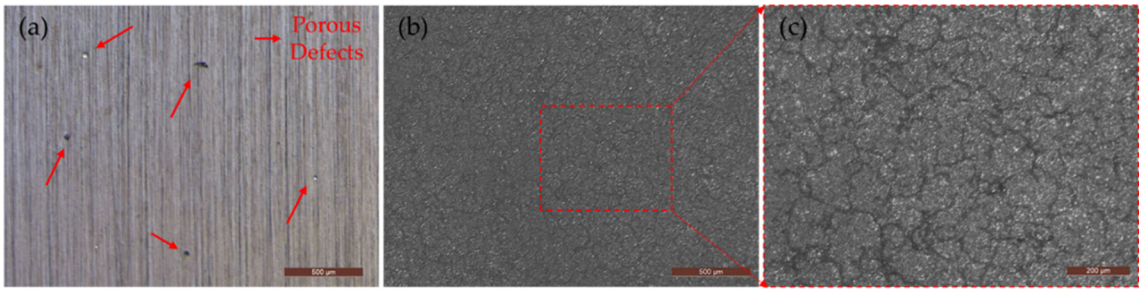

Fig. 5 Optical micrographs of the (a) CS and (b, c) CS + PEO surface morphologies

makes sense considering that the PEO buildup is uneven along the surface (Ref 46). In the case of the increasing S_{sk} parameter, it represents that there is a positive skewing along the surface, which likely was attributed to the visually extruded material shown in Fig. 4(e).

To further understand the change in surface morphology, optical and SEM micrographs were obtained. These findings can be seen in Fig. 5 and 6. From an optical perspective, evidence of porous defects can be found along the surface of the CS substrate (Fig. 5a). Based on our previous work, the porosity content of the CS coating is around 0.173% (Ref 19). However, upon PEO deposition, the CS + PEO sample effectively has no visual pores along the surface. Although the PEO film was not completely even, it appears that some form of the film was completely distributed along the exposed surface, as shown in Fig. 5(b). A magnified viewing of the film from Fig. 5(b) can be seen in Fig. 5(c). SEM micrographs of the CS and CS + PEO surfaces were also obtained to better understand the change in surface morphology, as shown in Fig. (6). For the CS surface (Fig. 6a), a similar texture as to what was shown in the optical micrographs (Fig. 5a) can be seen. An enlarged portion of the CS surface can be seen in Fig. 6b, which shows the presence of a porous defect. For the PEO film (Fig. 6c), it can be seen that a largely homogenous film was formed along the surface of the CS substrate. Micro-cracks can also be seen, which can usually suggest that the insulating characteristics of the deposited layer are hampered, which can result in non-uniform plasma discharging along the surface. This phenomenon is attributed to the leakage of current along these specific crack sites (Ref 47). Aside from these features, Fig. 6d shows sparse spherical nanostructured objects can be seen along the voided (i.e., non-dense) regions of the surface. Such a structure can act as evidence of severe bubble implosions from the plasma discharge/hydrogen evolution along the surface (Ref 44). A cross-sectional view of the PEO film at 550X and 1900X magnifications can be further seen in Fig. 7(a) and (b). It is

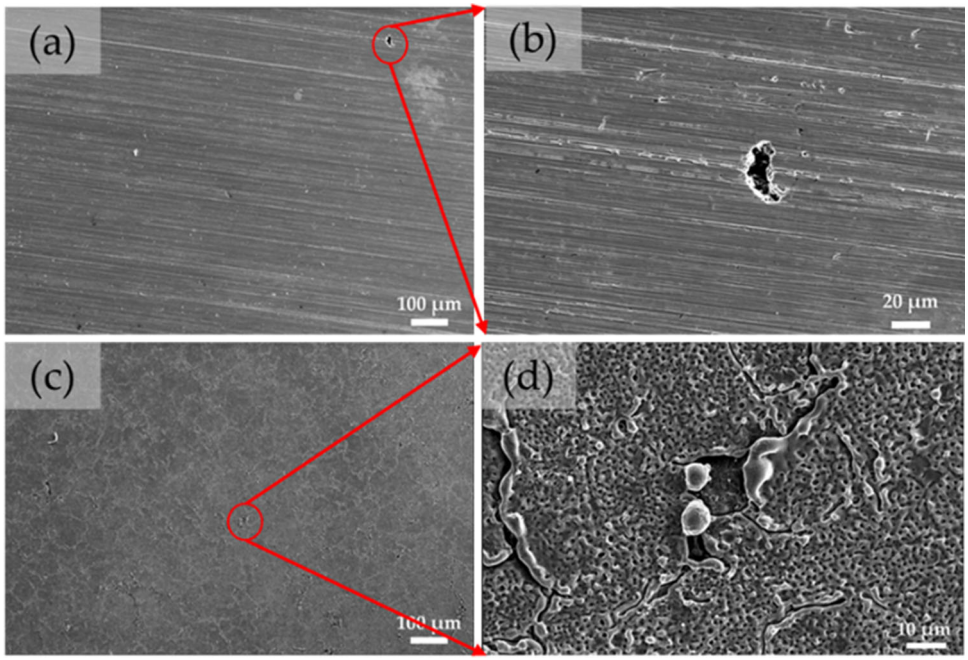

Fig. 6 SEM micrographs of the surface morphology of the (a, b) CS and (c, d) CS + PEO substrates

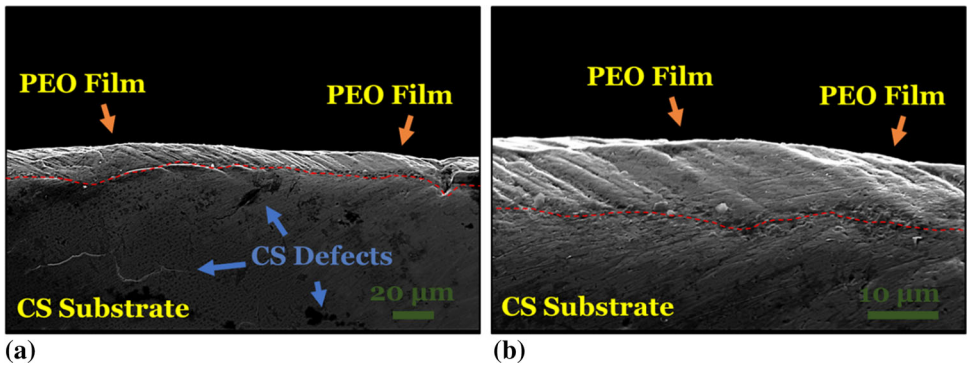

Fig. 7 Cross section SEM micrographs of the PEO film at (a) 550X and (b) 1900X magnifications

conspicuous to note that the film appears to be free from any obvious cross-sectional cracks, indicating that the coating is of good quality. Quantitatively, the average PEO film thickness was also found to be 12.30 ± 2.73 μm, indicating that sufficient deposition took place.

3.3 Phase and Chemical Composition

Aside from the physical characteristics, phase, and chemical observations were also made along the surface to confirm the presence of Al_2O_3 formation. In Fig. 8, an SEM image of the CS + PEO specimen (Fig. 8a) alongside the corresponding concentration of O (Fig. 8b), Al (Fig. 8c), Cr (Fig. 8d), Fe (Fig. 8e), Ni (Fig. 8f), and Mo (Fig. 8g) is shown. The peaks of the EDS spectra obtained from this imaged area are also shown in Fig. 8(h). It can be seen that Al and O are indeed present along the CS + PEO surface. However, their cumulative presence was fairly faint, which can indicate lackluster thickness along the surface (Ref 43). This finding can also likely be attributed to the non-uniform structure that was previously observed, as elements associated with the CS specimen (Fig. 9a-f) were also predominantly present. Additionally, the presence of such elements can also be evidence of a thin film along the surface. Nonetheless, the presence of such peaks indicates that Al_2O_3 was indeed deposited on the surface. For reference, the weight percentages of each element from Fig. 8 and 9 are listed in Table 3.

As a secondary source of information, XRD measurements were made along the surfaces of the CS and CS + PEO substrates. The corresponding XRD spectra for both specimens can be seen in Fig. 10. As can be seen, there is no visible detection of Al_2O_3 peaks along the surface. Rather, the phase characteristics of both specimens remain largely the same, being a γ/α duplex structure. Such findings validate that the presence of the aluminized layer was not significant enough to be shown in the XRD spectra. During PEO, it is usually expected that an aluminate-centric electrolyte will form the Al_2O_3 phase through the following chemical reaction (Ref 48):

$$2Al + 3O^{2-} \rightarrow Al_2O_3 + 6e^- \quad \text{(Eq 1)}$$

However, despite this expectation, the lackluster elemental results from Table 3 likely resulted in the absence of the Al_2O_3 characteristic phase. Interestingly enough though, the intensity

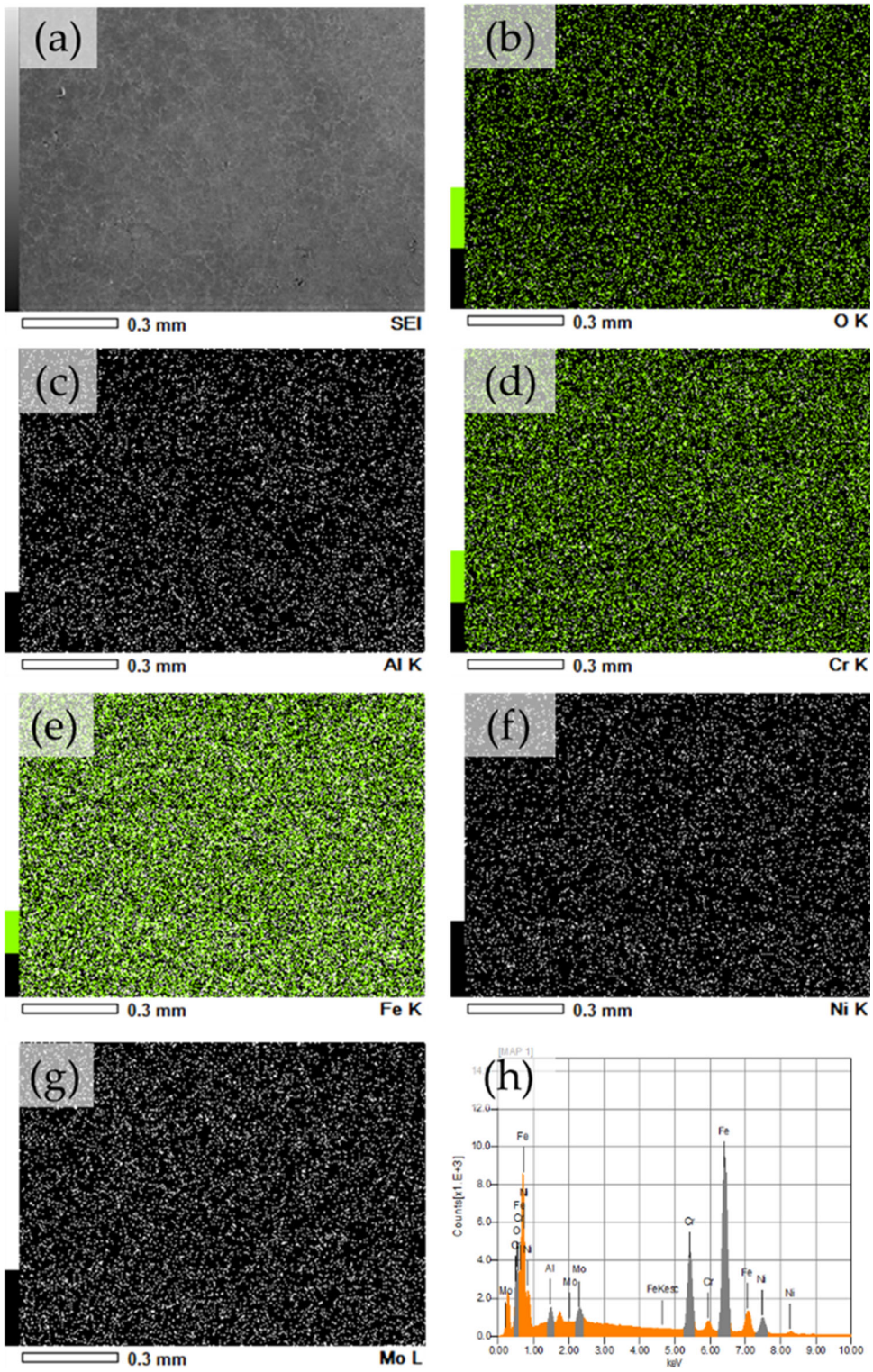

Fig. 8 (a) SEM micrograph of the CS + PEO substrate, alongside the EDS maps of the (b) O, (c) Al, (d) Cr, (e) Fe, (f) Ni, (g) Mo elements; (h) the corresponding EDS spectra obtained

of the α peak was reduced post-PEO. Although not necessarily pertinent to the PEO deposition, such a change indicates that some part of the α phase converted to the γ phase. Such an occurrence can be explained with the modified Johnson–Mehl–Avrami (JMA) equation for non-isothermal conditions, which suggests that rapid temperature rises can allow for the α phase to diffuse into the γ phase (Ref 49). In relation to the process used in this work, the immense thermal energy associated with the discharging channels from the electrochemical and plasmochemical reactions likely resulted in a rapid temperature rise

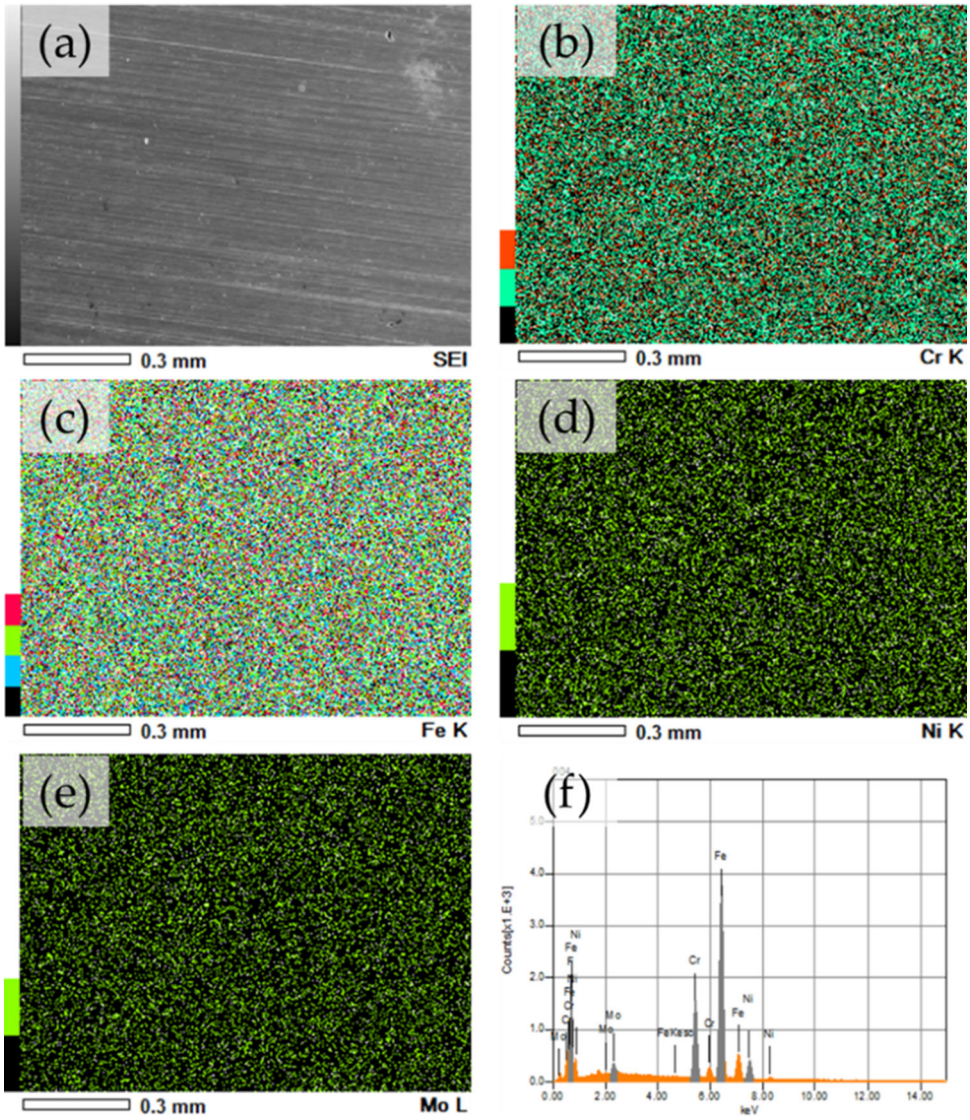

Fig. 9 (a) SEM micrograph of the CS substrate, alongside the EDS maps of the (b) Cr, (c) Fe, (d) Ni, (e) Mo elements; (f) the corresponding EDS spectra obtained

Table 3 The elemental composition of the CS and CS + PEO treated specimens measured by EDS

	Cr	Fe	Ni	Mo	Al	O
CS	17.38	66.16	10.57	3.36	…	…
CS + PEO	17.57	66.22	11.21	2.56	0.71	1.95

along the surface (as evident by the micro-cracks shown in Fig. 5 and 6) (Ref 50). Due to this finding, the heat generation likely allowed for such a phase change to occur (Ref 37, 51).

3.4 Electrochemical Characterization

3.4.1 Potentiodynamic Polarization Test. To validate the electrochemical feasibility of the formed coatings, the OCP and corresponding polarization curves of the CS and CS + PEO specimens in 3.5 wt.% NaCl solution are shown in Fig. 11. First assessing the OCP curves (Fig. 11a), the CS specimen stabilized at − 0.22 V versus SCE, whereas the CS + PEO specimen stabilized at − 0.17 V versus SCE. Generally, measuring the OCP acts as a key indicator of the dynamic equilibrium dissolution along the specimen surface. By having a less noble OCP, a sample tends to be more susceptible to corrosion degradation (Ref 52). With the CS + PEO specimen having a more noble potential, it has a lesser tendency for corrosion, unlike the CS specimen. After OCP stabilization, the PDP curves for each specimen were obtained, as shown in Fig. 11b. Key variables such as the corrosion potential (E_{corr}), corrosion current density (I_{corr}), and corrosion rate (mm/yr) are shown in Table 4. It can be seen that with the uncoated specimen, the E_{corr} and I_{corr} values were measured at − 0.48 V versus SCE and 2.93×10^{-5} A cm^{-2}. However, when observing the CS + PEO substrate, the E_{corr} and I_{corr} values both decreased to − 0.28 V versus SCE and 4.73×10^{-5} A cm^{-2}. Through these data, the corrosion rate was calculated through the following relation (Ref 42):

$$CR = \frac{I_{corr} KEW}{dA} \quad \text{(Eq 2)}$$

where CR represents the corrosion rate (mm/yr), K is the corrosion rate constant (3272), EW is the equivalent weight, d is the density of the material (g cm_{-3}), and A is the working area (cm^2). Based on this relation, it was found that the corrosion rates for the CS and CS + PEO specimens is 3.04 and 0.49 mm/yr. These findings show that the CS + PEO substrate has a greater corrosion resistance than the CS substrate in NaCl solution.

To better understand the change in corrosion degradation, optical profiles of the corroded CS and CS + PEO surfaces were obtained. These profiles are shown in Fig. 12, with two images of the CS corroded surface being shown in Fig. 12(a) and (b) and the CS + PEO corroded surface being shown in Fig. 12(c) and (d). For the CS substrate, surface deterioration can be seen due to the rusted-like discoloration along the surface. Evidence of surface pitting can be seen, especially in Fig. 12(a). For the CS + PEO specimen, the amount of visual degradation appears to be much less, as the PEO film is still in contact. A few pits can be observed along specific regions along the surface, which indicates that the Cl^- ions did penetrate the PEO film.

Understanding these characteristics, the change in pitting morphology and formation was also investigated by taking 3D profile images along the pitted surfaces. As shown in Fig. 13, there is a stark difference between the pit formation of the CS (Fig. 13a-c) and CS + PEO (Fig. 13e-f) specimens. In the case of the CS substrate, the formed pits appear to be larger in their structure (Fig. 13a,b), which can be associated with the intrinsic porous defects from the CS process. These observations were confirmed through 2D-line profile measurements, of which the three deepest pits were assessed (Fig. 13c). Collectively, their depths were relatively similar, with an average pit depth measuring at -63.27 ± 11.44 μm. In the case of the CS + PEO substrate, there were nearly no pits formed along the surface. In fact, from the existing pits that did form along the surface, their magnitude in both width and depth was drastically reduced. Out of the three deepest pits, their average depth was measured at -38.72 ± 30.67 μm, with the high standard deviation being due to the presence of only relatively deep pits compared to the third pit. Nonetheless, the CS + PEO specimen had a 38.80% cumulative reduction in pitting depth. For reference, the measured depths for all pits alongside their average and standard deviations can be seen in Table 5.

With this being said, although the pitting depth can provide insights into the surface's tendency of localized corrosion, the quantity of pits formed should also be considered. To do so, three micrographs of each corroded surface were obtained. By doing so, the number of pits formed along each surface can be represented. In each micrograph, the formed pits were highlighted in red using ImageJ (Ref 53) software. These findings

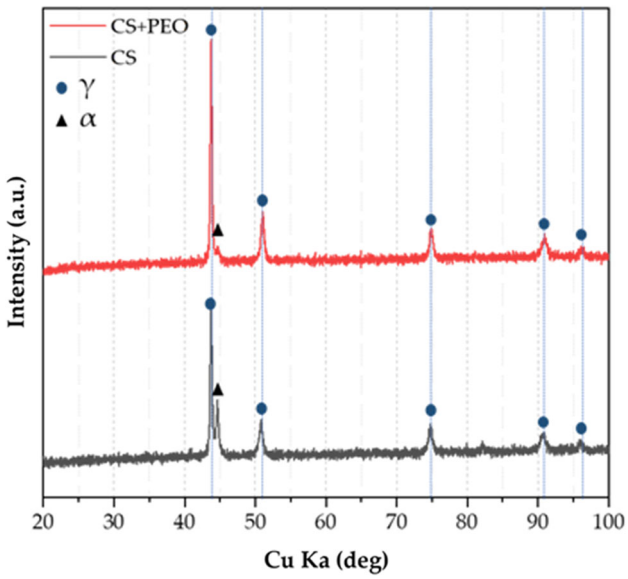

Fig. 10 The XRD spectra of the CS and CS + PEO substrates

Table 4 The electrochemical characteristics of the CS and CS + PEO substrates obtained from the PDP curves in 3.5 wt.% NaCl solution

	E_{corr}, V	I_{corr}, A cm^{-2}	Corrosion rate, mm/yr
CS	− 0.48	2.93×10^{-5}	3.04
CS + PEO	− 0.28	4.73×10^{-6}	0.49

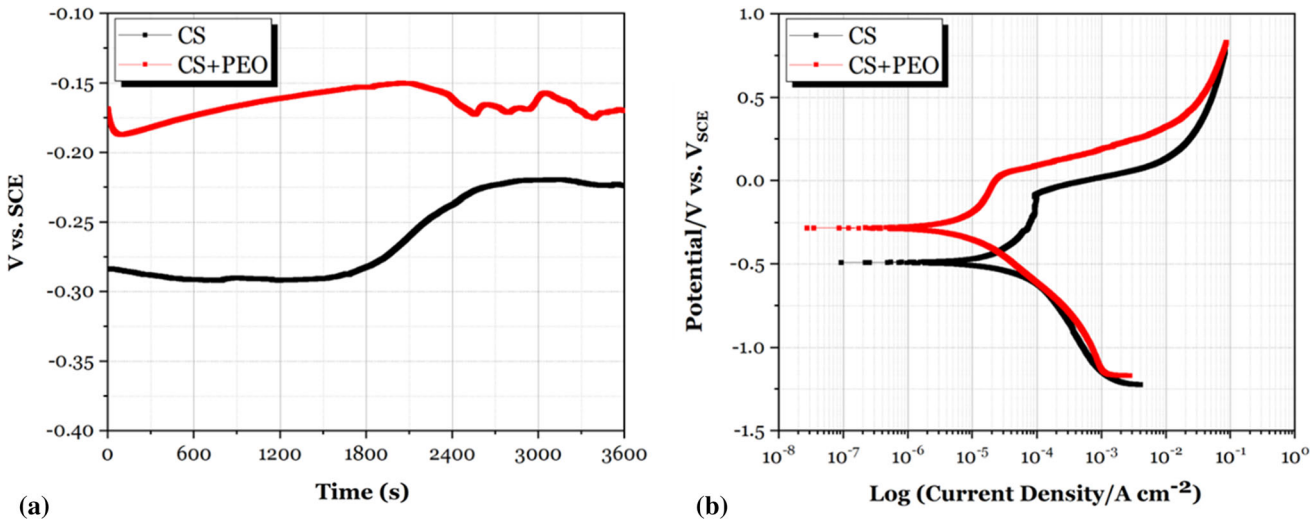

Fig. 11 The (a) OCP and (b) PDP characteristics of the CS and CS + PEO specimens in 3.5 wt.% NaCl solution

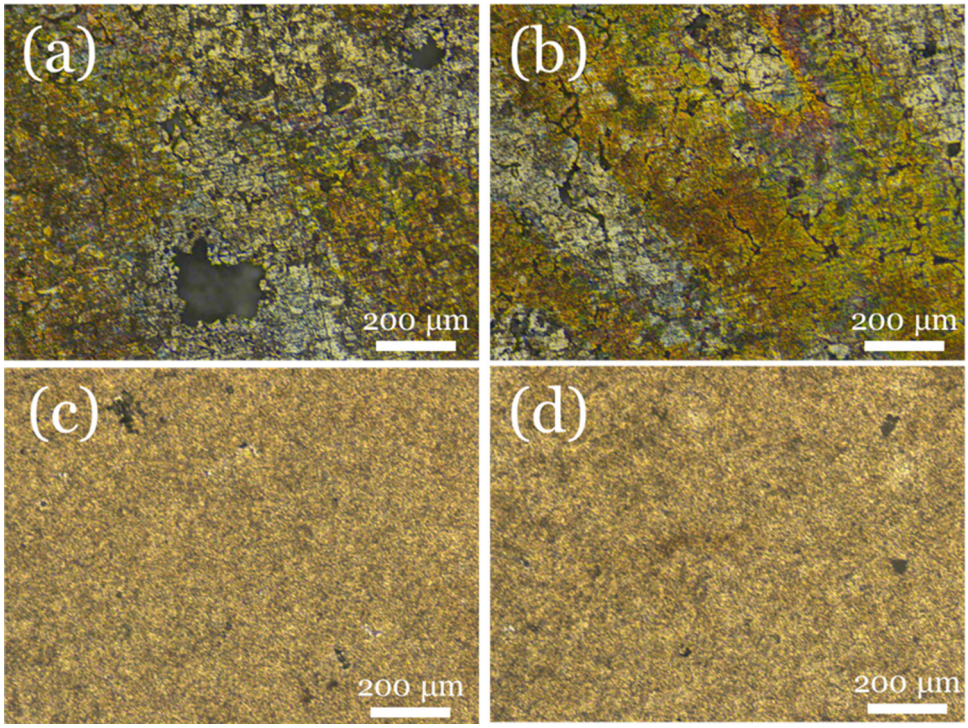

Fig. 12 Optical micrographs of the (a, b) CS and (c, d) CS + PEO corroded surfaces after PDP testing in 3.5 wt.% NaCl solution

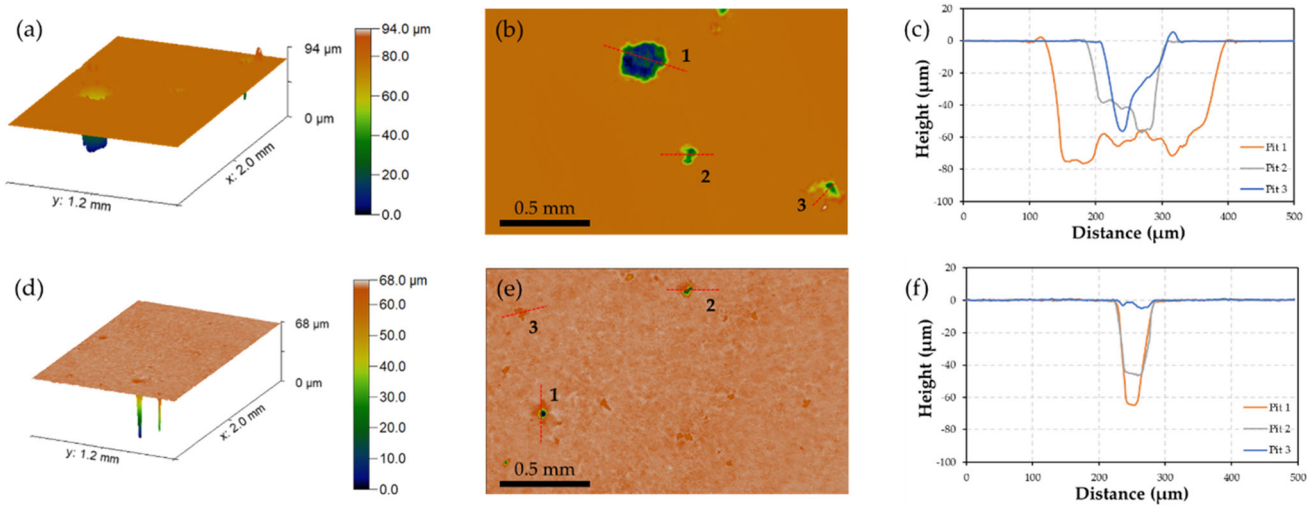

Fig. 13 3D profilometer imaging of the (a-c) CS and (d-f) CS + PEO substrates in 3.5 wt.% NaCl solution

Table 5 The various recorded pit depths of the CS and CS + PEO substrates in 3.5 wt.% NaCl solution

	Pit 1 depth, μm	Pit 2 depth, μm	Pit 3 depth, μm	Average depth, μm	SD, μm
CS	− 76.47	− 57.12	− 56.21	− 63.27	11.44
CS + PEO	− 64.80	− 46.43	− 4.92	− 38.72	30.67

are shown in Fig. 14. It can be seen that for the CS specimen (Fig. 14a-f), the pits formed appear to be quite large in nature, validating the pitting depth analysis previously made. For the CS + PEO specimen (Fig. 14g-l), the sizing of the pits appears to decrease. However, there appears to be a greater amount of individual pits formed along the surface. Quantifiably, from these micrographs, the CS specimen had a total of 16 pits formed, whereas the CS + PEO specimen had a total of 29 pits formed. The greater amount of formed pits can be attributed to the roughened surface, as the Cl^- ions can more easily

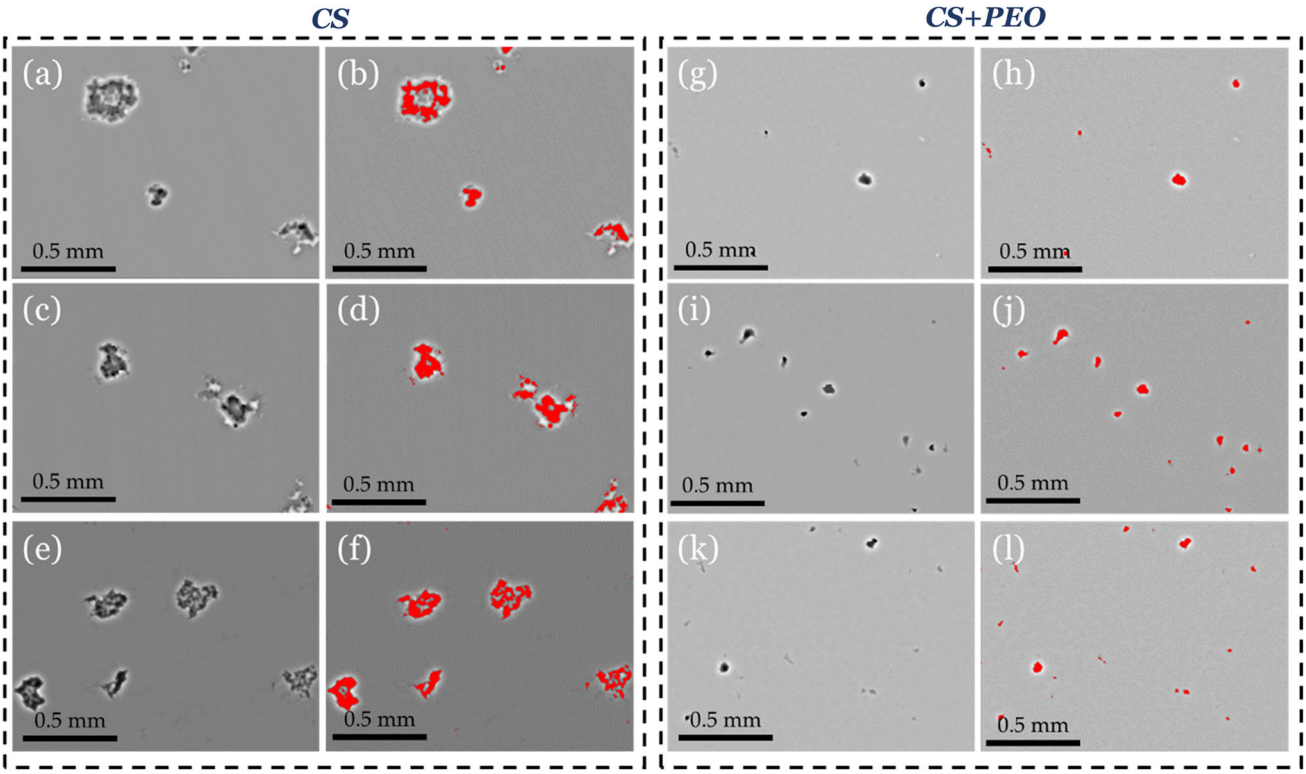

Fig. 14 The pitting morphology, with and without highlights, of the (a-f) CS and (g-l) CS + PEO specimens formed from 3.5 wt.% NaCl solution

penetrate into specific localized spots (Ref 54). Nonetheless, with their general sizing being much less, the area percentage of surface porosity was calculated and averaged. It was found that the CS specimen had a pitting area average of 2.60 ± 0.64%, whereas the CS + PEO specimen had a pitting area average of 0.40 ± 0.15%. These findings show that despite the higher number of individual pits formed, the overall area of the pits appears to be more severe for the CS specimen.

For the HBSS solution, the corresponding OCP and PDP measurements for the CS and CS + PEO substrates are shown in Fig. 15. For the OCP measurements (Fig. 15a), the CS + PEO substrate had the noblest OCP, measuring at − 0.13 V versus SCE, whereas the CS substrate measured at − 0.22 V versus SCE. In each case, the OCP appears to be largely in electrochemical equilibrium. It can also be noted that for the CS substrate, there is some type of perpetuation that occurs throughout OCP testing. Such results tend to suggest that the passive film is exhibiting a meta-stable-like behavior, of which there is a constant degree of breakdowns and repassivations (Ref 55). This phenomenon is likely due to the influence of pores along the surface, as they can act effectively to weaken the passive film along the surface. For the PDP conditions (Fig. 15b), the E_{corr} and I_{corr} values appear to follow a similar trend as the NaCl testing conditions, with the corrosion rate for the CS and CS + PEO sample being 0.66 and 0.23 mm/yr. Comparative to the NaCl conditions, the corrosion rate appears to be drastically reduced. This explanation can be attributed to the lesser quantity of chloride ions in the HBSS solution, as the NaCl solutions tend to be more aggressive in nature. For reference, these findings are shown in Table 6.

Various optical profiles of the CS and CS + PEO surfaces post-PDP testing were additionally obtained. These profiles can be seen in Fig. 16, with the CS specimen being in Fig. 16(a) and (b) and the CS + PEO specimen being in Fig. 16(c) and (d). Similar to the optical micrographs obtained for the 3.5 wt.% NaCl testing conditions, the presence of surface degradation via discoloration and surface pitting can be seen. For the CS + PEO specimen, the film also appears to be intact. Relative to the CS specimen, there appears to be much less degradation, confirming that lesser corrosion degradation took place.

To further understand the change in pit morphology, the same analytical approach used for the NaCl substrates was utilized. The findings are shown in Fig. 17. It can be seen that the pits for the CS specimen (Fig. 17a-c), the sizing of the pits appears to be relatively the same. For the CS + PEO specimen (Fig. 17d-f), the sizing of the pits greatly decreases in size. To confirm this visual observation, the depths of the pits were measured and tabulated in Table 7, where the average pit depth for the CS specimen being − 43.62 ± 0.04 μm whereas the CS + PEO specimen was at − 5.97 ± 1.19 μm. Relative to the NaCl pits, the size and depth of both the CS and CS + PEO pits were significantly less, which also follows suit with the reduced corrosion rates.

The number of pits alongside the respective area percentage average for the CS and CS + PEO specimens in HBBS solution can be seen in Fig. 18. The CS micrographs are shown in Fig. 18a-f, whereas the CS + PEO micrographs are shown in Fig. 18g-l. Similar to the NaCl testing conditions, the sizing of the pits appears to be much larger for the CS specimen, whereas the frequency of pits appears to be greater for the CS + PEO specimen. The number of pits calculated for the CS specimen consisted of 7, whereas the for CS + PEO specimen had 22. Additionally, the pitting area percentage calculation for the CS

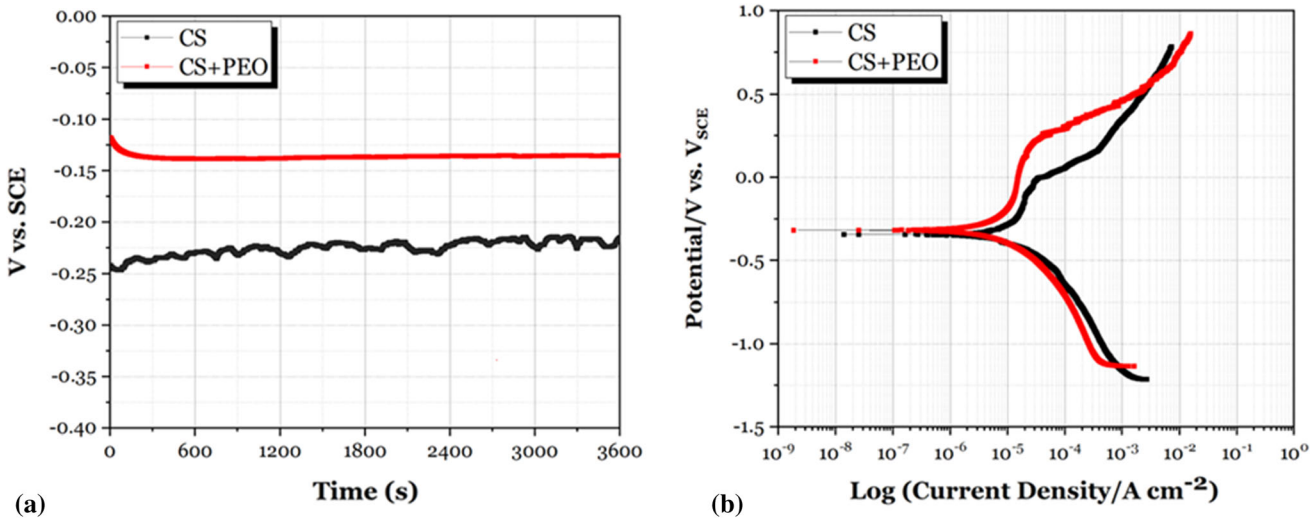

Fig. 15 The (a) OCP and (b) PDP characteristics of the CS and CS + PEO specimens in HBSS solution

Table 6 The electrochemical characteristics of the CS and CS + PEO substrates obtained from the PDP curves in HBSS solution

	E_{corr}, V	I_{corr}, A cm^{-2}	Corrosion rate, mm/yr
CS	− 0.34	6.34×10^{-6}	0.66
CS + PEO	− 0.31	2.24×10^{-6}	0.23

specimen was 0.45 ± 0.15%, whereas the CS + PEO specimen had 0.14 ± 0.02%. Following a similar trend as the NaCl testing conditions, the same takeaways for surface roughness and pit initiation can be taken away.

3.4.2 Electrochemical Impedance Spectroscopy. Although PDP tests can provide useful information regarding the variation in corrosion degradation, EIS experiments can provide greater insights into the resistance of the PEO coating to the NaCl and HBBS solutions. To do so, a single equivalent

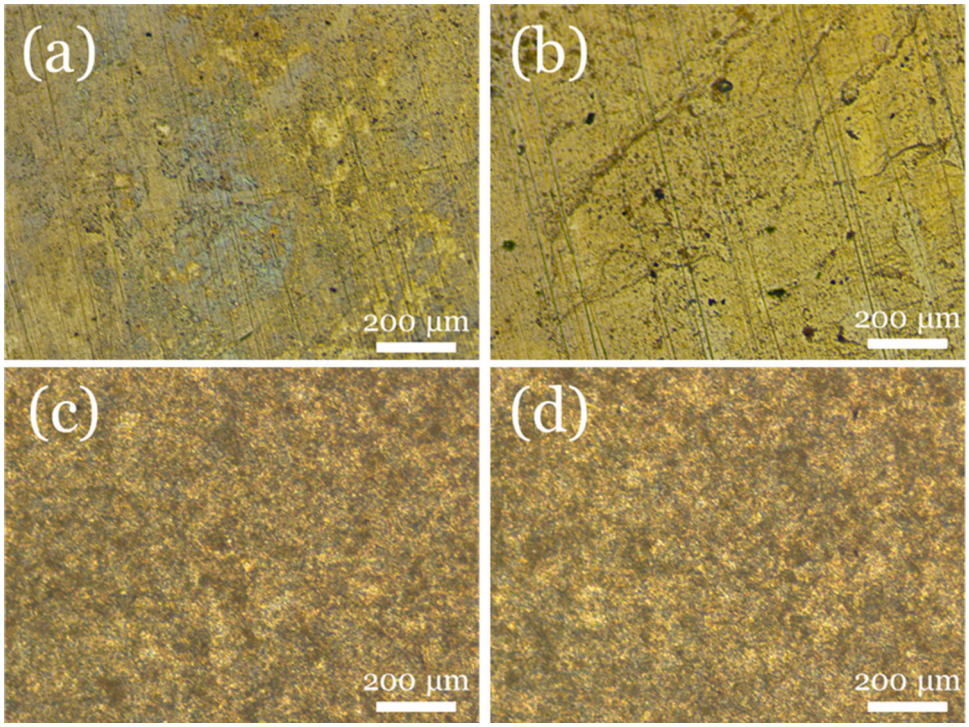

Fig. 16 Optical micrographs of the (a,b) CS and (c,d) CS + PEO corroded surfaces after PDP testing in HBBS solution

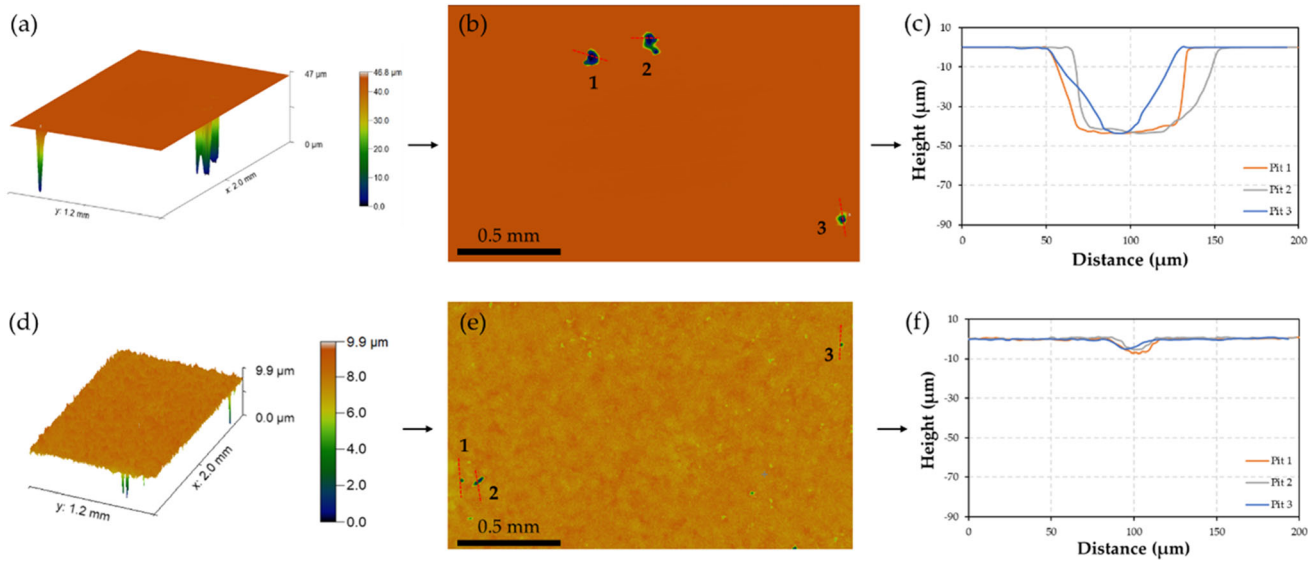

Fig. 17 3D profilometer imaging of the (a-c) CS and (d-f) CS + PEO substrates in HBSS solution

Table 7 The various recorded pit depths of the CS and CS + PEO substrates in HBSS solution

	Pit 1 depth, μm	Pit 2 depth, μm	Pit 3 depth, μm	Average depth, μm	SD, μm
CS	− 43.61	− 43.67	− 43.59	− 43.62	0.04
CS + PEO	− 7.32	− 5.49	− 5.09	− 5.97	1.19

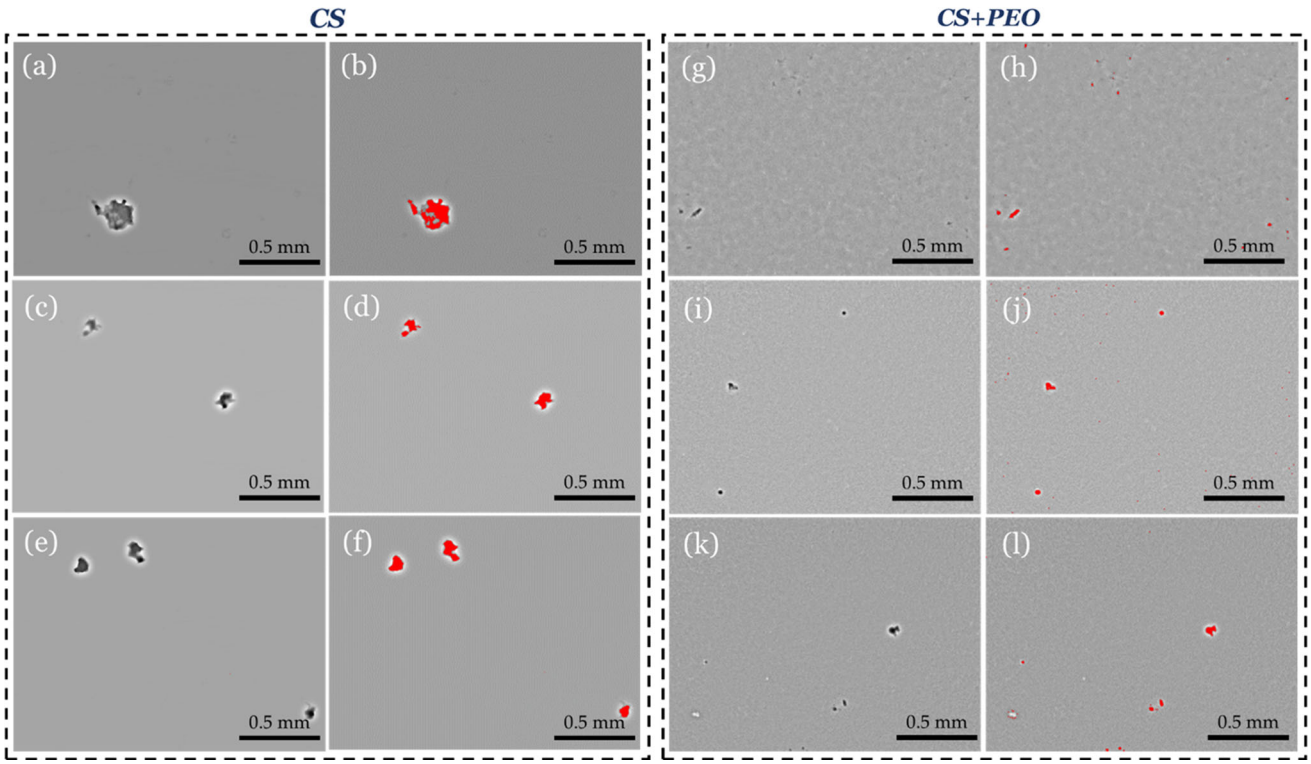

Fig. 18 The pitting morphology, with and without highlights, of the (a-f) CS and (g-l) CS + PEO specimens formed from HBBS solution

electrical circuit (EEC) was employed to fit the impedance spectra for both the CS and CS + PEO specimens. A visualization of this circuit can be seen in Fig. 19, where its fitting relative to the CS (Fig. 19a) and CS + PEO (Fig. 19b) surfaces is shown. In the EEC, two-time constants, C_c and C_{dl}, were applied to represent the outer and inner layers of the CS and CS + PEO surfaces. In this context, the outer layer of the CS surface is the oxide film, whereas the outer layer of the CS + PEO surface is the PEO film. The inner layer for both specimens consists of the CS surface. The resistance of these layers is also represented by R_{po} (outer layer) and R_{ct} (inner layer), whereas the resistance to the electrolytic solution is R_s. Although factors such as uneven oxide film formation (due to porosity for the CS specimen) and roughened surface topography (due to the PEO film) can complicate the EEC fitting, the usage of two-time constants can safely minimize potential errors. Furthermore, this EEC has been widely used for steel substrates both with and without PEO coatings (Ref 56, 57).

In NaCl conditions, the Nyquist plot (Fig. 20a) shows that both the CS and CS + PEO substrates hold similar semicircular features. However, the size of the capacitance curve for the CS + PEO specimen is larger than that of the CS substrate, indicating that the charge transfer resistance is improved (Ref 57). The broadened phase angle peak the CS + PEO specimen shown in Fig. 20b also indicates that the corrosion resistance was greater than the CS specimen (Ref 58). Table 8 depicts the electrical parameters obtained from the EEC for both the CS and CS + PEO specimens. Typically, to quantifiably determine the polarization resistance, R_{po} and R_{ct} can be used to determine the corrosion resistance and stability of the outer and inner layers of the CS/CS + PEO surfaces. The overall corrosion potential (R_{pol}) can further be determined by the following relation:

$$R_{pol} = R_{po} + R_{ct} \quad \text{(Eq 3)}$$

Which combines the individual R_{po} and R_{ct} components. For the CS specimen, R_{pol} was found to be $1.83 \times 10^4\ \Omega\ cm^2$ whereas for the CS + PEO specimen, R_{pol} was found to be $4.72 \times 10^4\ \Omega\ cm^2$. Based on these findings, it can be seen that the CS + PEO specimen exhibits the greatest charge transfer resistance.

In the HBBS solution, the impedance modulus of the CS + PEO specimen in the Nyquist plot (Fig. 21a) also appears to be greater than that of the CS specimen. Furthermore, in Fig. 21b, the CS + PEO specimen also has a broadened phase angle, which also suggests that the CS + PEO specimen has a greater corrosion resistance. Table 9 depicts the obtained electrical parameters for both specimens. Evaluating their R_{pol} values, the CS specimen had an R_{pol} of $3.28 \times 10^4\ \Omega\ cm^2$, whereas the CS + PEO specimen had an R_{pol} of $2.90 \times 10^5\ \Omega\ cm^2$. These findings further support the PDP plots previously discussed.

4. Discussion

4.1 Coating Formation Mechanism

To understand the findings from this work, it is crucial to first understand the formation of the PEO film along the CS surface. Among the existing literature (Ref 38, 59), there has been some understanding of the formation mechanisms associated with the deposition of Al_2O_3 on PEO SSs. In essence, the role of the aluminate electrolytes is to form a barrier that will allow for the anodic discharges to take place (Ref 60). By having a continual stream of steady and uniform discharges, the anion species of $Al(OH)^{4-}$ begins to migrate toward the nearby discharge channels (via electric fields) and is effectively bonded with the working surface (Ref 35). Such a process can be described by the following equations (Ref 39):

$$\left[Al(OH)_4\right]^- \rightarrow \left[Al(OH)_4\right]^{\circ} + e \rightarrow \left[Al(OH)_3(OH)^{\circ}\right] \quad \text{(Eq 4a)}$$

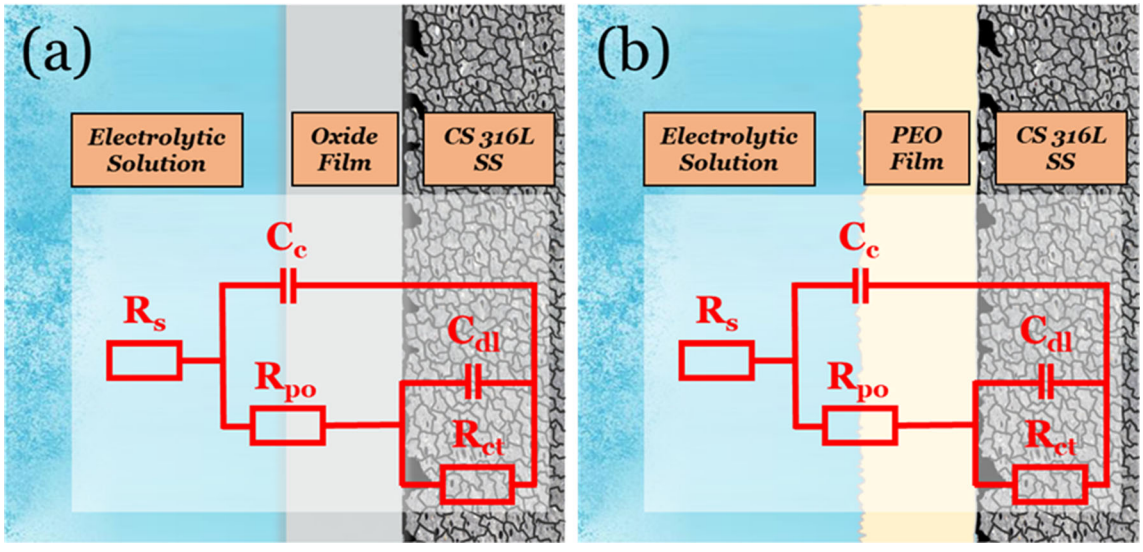

Fig. 19 The EECs used to fit the impedance data for the (a) CS and (b) CS + PEO specimens

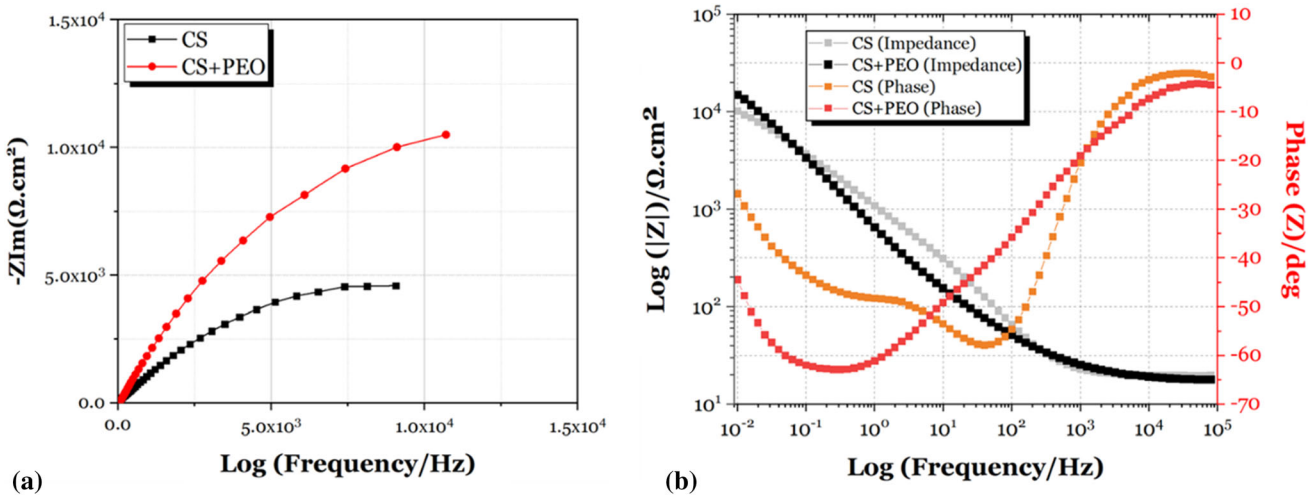

Fig. 20 The (a) Nyquist and (b) Bode plots of the CS and CS + PEO specimens in 3.5 wt.% NaCl solution

Table 8 The EEC values obtained from EIS testing for the CS and CS + PEO specimens in 3.5 wt.% NaCl solution

	R_s, Ω cm^2	R_{ct}, Ω cm^2	C_{dl}, F cm^{-2}s^{n-1}	n	R_{po}, Ω cm^2	C_c, F cm^{-2}s^{n-1}	n
CS	19.55	1.79×10^4	2.80×10^{-4}	0.582	492.2	7.06×10^{-5}	0.850
CS + PEO	17.99	4.71×10^4	1.75×10^{-4}	0.765	118.3	2.28×10^{-4}	0.692

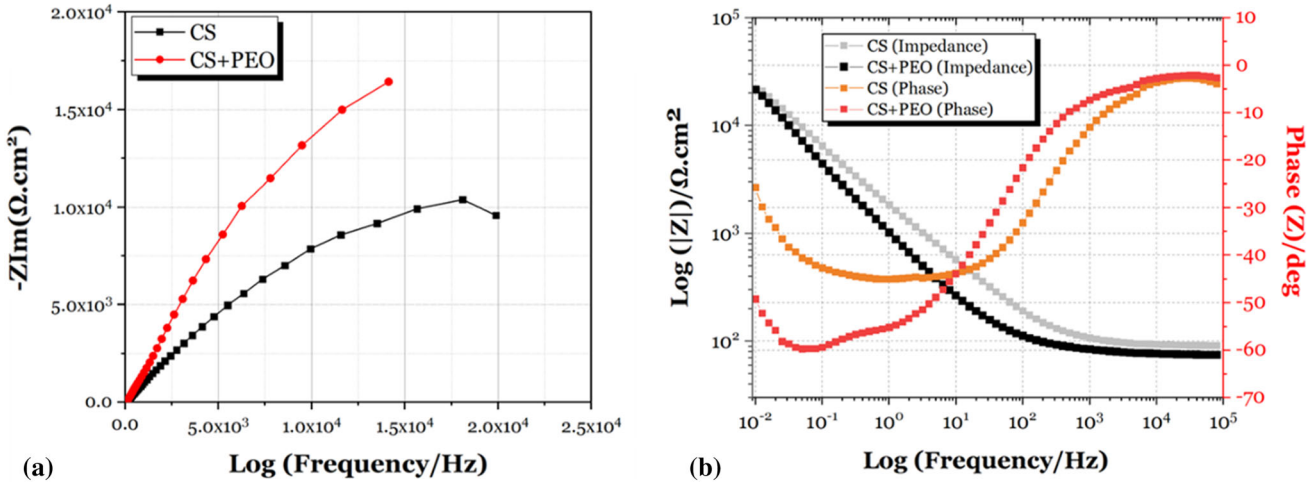

Fig. 21 The (a) Nyquist and (b) Bode plots of the CS and CS + PEO specimens in HBBS solution

Table 9 The EEC values obtained from EIS testing for the CS and CS + PEO specimens in HBBS solution

	R_s, Ω cm^2	R_{ct}, Ω cm^2	C_{dl}, F cm^{-2}s^{n-1}	n	R_{po}, Ω cm^2	C_c, F cm^{-2}s^{n-1}	n
CS	89.51	2.85×10^4	8.25×10^{-5}	0.766	4.31×10^3	1.27×10^{-4}	0.639
CS + PEO	77.03	4.41×10^3	2.74×10^{-2}	0.493	2.86×10^5	2.98×10^{-4}	0.661

$$2\left[Al(OH)_3(OH)^{\circ}\right] \rightarrow 2\left[Al(OH)_3 \cdot H_2O_2\right] \rightarrow 2Al(OH)_3 + H_2O + {}^1/_2O_2 \quad \text{(Eq 4b)}$$

$$\left[Al(OH)_4\right]^- \rightarrow Al(OH)_3 + {}^1/_2O_2 + 2H_2O + e \quad \text{(Eq 5)}$$

$$\left[Al(OH)_4\right]^- \rightarrow Al_2O_3 + {}^1/_2O_2 + 4H_2O + 2e \quad \text{(Eq 6)}$$

However, this process is under the assumption that a traditionally manufactured material (via techniques such as casting and hot rolling) is being used. As aforementioned, the crystalline structures of CS materials tend to be quite higher than traditionally manufactured materials due to the severe plastic deformation induced by the deposition process (Ref 61). Such an implication can result in a reduction of thermal conductivity, which can negatively impact the overall coating thickness (Ref 62). To explicate, in highly crystalline structures, the intragranular thermal transmission property of the grains reduces the phonon mean free path (PMFP) during the heat transfer process. Due to this reduction, the degree of phonon scattering increases (Ref 63). In relation to the PEO process, the decrease in thermal conductivity will result in a shortened electric field (during plasma discharging), thus resulting in a lesser deposition of $Al(OH)^{4-}$ anions (Ref 64). This phenomenon was observed in the present work, in which a non-uniform film was formed along the surface. However, to further validate this claim, the FWHM of the XRD peaks pre-PEO specimen (Fig. 10) were observed and used to calculate the crystallite size of the CS substrate via the Williamson–Hall method. It was found that the crystallite size of the CS substrate was measured to be 14.68 nm. Compared to reported crystallite size findings for traditionally casted steel (which has been reported to be within the 130 to 150 nm range [Ref 65, 66)], this explanation can be further validated.

Another factor to also consider is the general surface morphology of the CS substrate. Reflecting on the discussion of Section 3.2, the porous surface of the CS substrate can also negatively impact the flow of the electrical current during PEO deposition (Ref 67). This idea can be tied to the characteristics of the aluminate oxide film along the surface. With the presence of pores, the aluminate oxide film becomes unstable, due to its lesser relative thickness. These areas can act as electrical-sensitive sites, of which electrical breakdown can occur. In such a case, a large degree of the current is effectively leaked, thus resulting in an uneven plasma formation along the surface. From a visual standpoint, the cracked structure from Fig. 5 and 6 also indicates such an occurrence. Although outside of the scope of this work, this finding can also explain why no voltage breakdown took place, as the sporadic formation of vapor plumes could not form a steady state to allow such an occurrence from happening. Nonetheless, these findings insinuate that various voltage leakages occurred during PEO deposition, which further contributed to the uneven film seen in this work.

To further understand these points, a schematic of the coating forming mechanism is shown in Fig. 22. Specifically, it shows how the existing aluminate anions (Fig. 22a) in the solution deposit themselves along the surface of the CS substrate, thus resulting in the formation of a barrier (Fig. 22b,c). After the surface undergoes plasma discharging (Fig. 22d), an Al_2O_3 layer is formed (Fig. 22e). However, due to the influence of pre-existing pores and a highly crystalline surface, a non-uniform and thin film was applied. However, despite its formation, it demonstrates that there is great future potential for more effectively depositing thicker and more uniform films for valve-based CS components.

4.2 Electrochemical Mechanism

From an electrochemical perspective, the corrosion rate for the PEO substrates was lesser than that of the CS specimen. To understand such a finding, it is important to consider a few key factors. These factors lie with "postponing" and "blocking" effects enabled by the existing Al_2O_3 film (Ref 35). Although non-uniform, the general chemical stability of Al_2O_3 (accompanied by influencing iron oxides) allows for an insulating type of effect along the surface (Ref 68). This effectively "blocks" the corrosive species from penetrating the CS surface, thus leading to an overall lessened corrosion rate. This was evident for both the NaCl and HBBS solutions, as their respective corrosion rates were lesser than that of the CS specimen. However, the thinner regions of the Al_2O_3 film can be susceptible to accelerated dissolution rates, which resulted in the greater formation of surface micro-pits. The interactions of surface roughness also likely played a role in this occurrence, as the total number of pits of the CS + PEO specimen in NaCl and HBBS solutions was greater than the CS specimen. Such degradation in chloride environments (which are present in the two tested solutions) can be explained by the general reaction (Ref 69):

$$Al^{n-}\left|\text{oxide} + V_O^{n+} + Cl^-(aq) \rightarrow Al^{(m)-}\right|\text{oxide} + Cl_{Vo}^{m+} + e^- \quad \text{(Eq 7)}$$

However, despite the higher quantity of individual pits formed along the surface, due to some presence of the film existing within the exposed area, the corrosive species of both solutions were effectively "postponed," which resulted in smaller pits along the CS + PEO surface. In NaCl conditions, the greater amount of Cl^- ions resulted in more severe pits than the HBBS conditions. Nonetheless, when these micro-pits were formed along the surface, the surrounding Al_2O_3 regions likely assisted with potential metastable film formations, which prevented deep penetration, as seen in the pitting depth analysis.

To better visualize this mechanism, a visual schematic of the change in the pitting mechanism for the CS and CS + PEO is shown in Fig. 23. For the CS substrate (Fig. 23a), it can be seen that the presence of Cl^- ions can attach pore-sensitive regions, thus resulting in unwanted pitting. However, when PEO deposition is applied (Fig. 23b), it can be seen that the formation of the Al_2O_3 film can effectively cover the pores and allow for a greater enhancement of the oxide film, which can mitigate the issue of pitting corrosion. In total, these results show that despite room for further PEO optimization, there is great feasibility for the applicability of enhanced corrosion resistance for CS 316L SS.

5. Conclusions

In this work, the deposition and electrochemical mechanisms associated with PEO-deposited Al_2O_3 on CS 316L SS were investigated. The conclusions are as followed:

1. The *j–U* characteristics from PEO deposition indicated a gradual increase in current density as a function of applied voltage. Based on visual observations, this finding suggests that a non-uniform distribution of the plasma discharges took place along the surface. The optimized voltage that was used for the remaining portion of this work was 400 V.
2. The overall surface roughness of the substrate increased post-PEO deposition. This increase in roughness was also accompanied by an increase in skewness and kurtosis. Upon closer observation, microcracks were present along the surface, suggesting that current leakage took place.

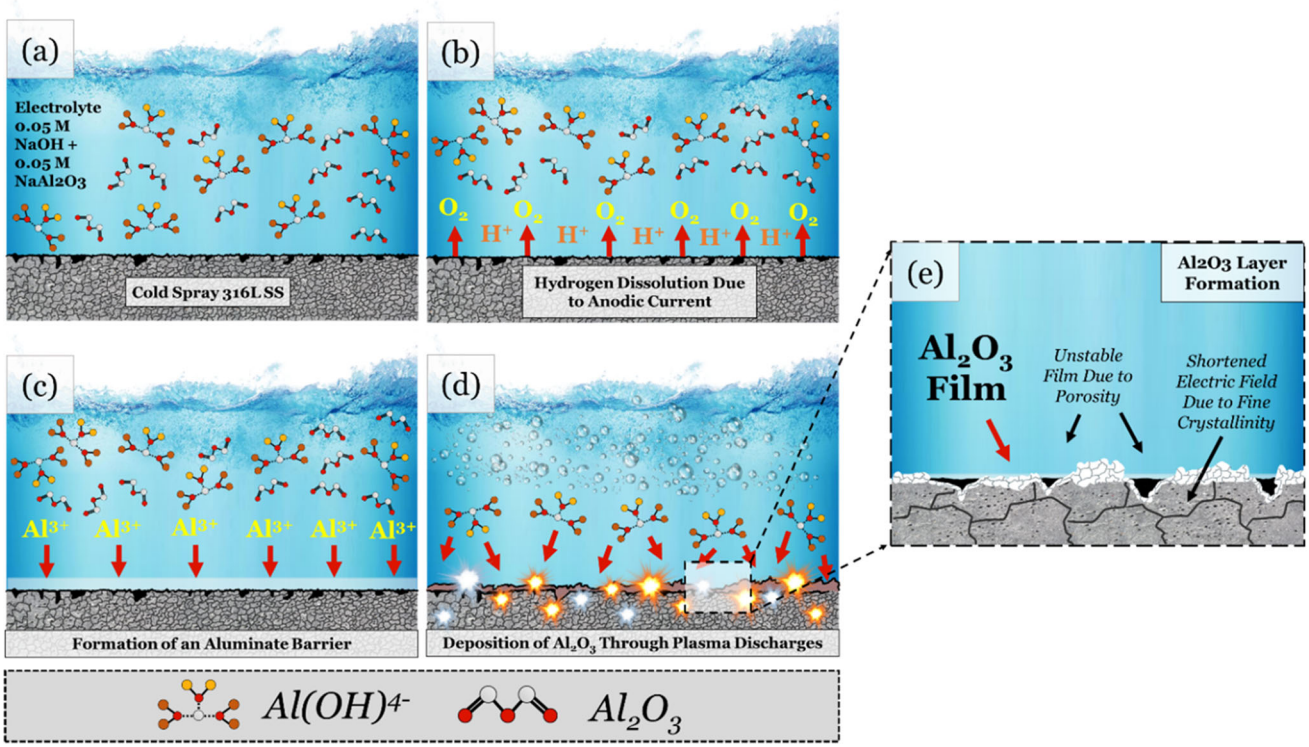

Fig. 22 A visual schematic of the PEO deposition mechanism for the CS SS substrate starting at the (a) pre-PEO state, then progressing with (b) applied anodic current to (c) form an aluminate barrier that undergoes (d) plasma discharging and eventual (e) Al_2O_3 deposition

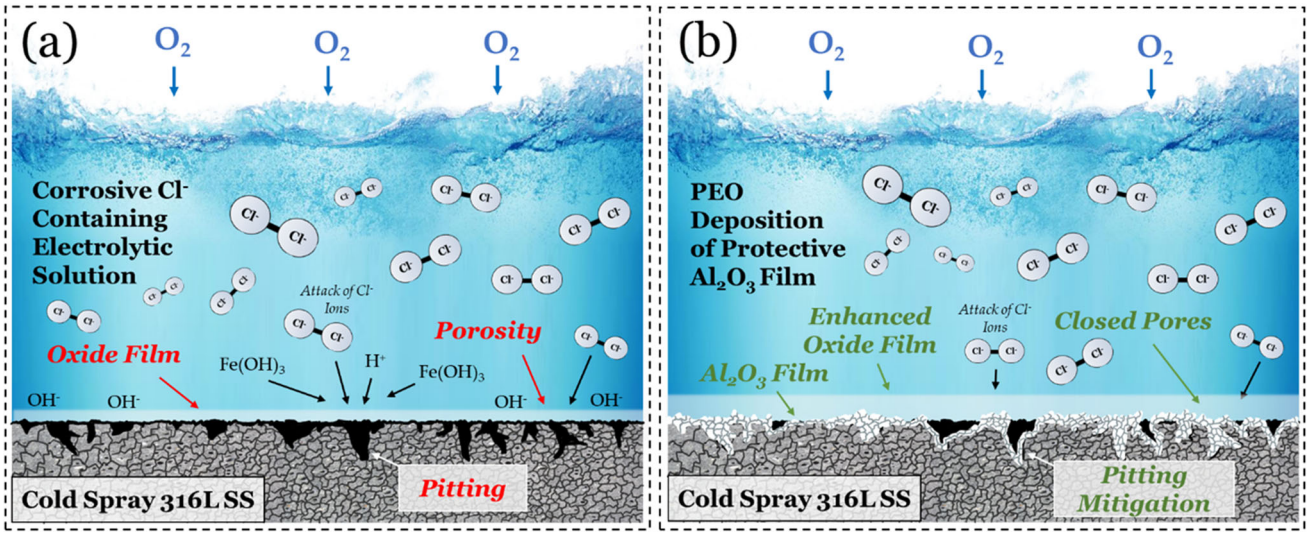

Fig. 23 A schematic of the pitting mechanism for the (a) CS and (b) CS + PEO specimens

3. Elemental analysis of the surface confirmed that there was a presence of a Al_2O_3 PEO film. However, their characteristic peaks were relatively faint, further suggesting that non-uniform film deposition took place.
4. PDP tests demonstrated that the corrosion rate for the CS and CS + PEO specimens decreased in both 3.5 wt.% NaCl and HBSS solutions. The severity of surface pitting was also less severe for the CS + PEO specimen in both solutions. These findings are further supported by the improvement in charge transfer resistance found from EIS testing.
5. Collectively, the coating formation mechanisms were influenced by reduced thermal conductivity (due to the extremely refined crystalline structure) and surface porosity. Due to their influence, the surface was unable to form a uniform film. Regarding the corrosion mechanisms, the decrease in corrosion rate can be attributed to the postponing and blocking effect from the Al_2O_3 film. Due to the increase in surface roughness, a greater amount of individual pits were formed along the CS + PEO surfaces. However, the depth and overall sizing were much less than the CS

specimen. This finding can be due to the densifying nature of the PEO film (despite the non-uniformity) and the chemical stability of the existing Al_2O_3 film, thus reducing the pitting susceptibility of the CS + PEO surface.

Based on these findings, it can be confirmed that there is a feasibility of applying PEO coatings on CS SS components. However, due to the highly refined surface and porous structure, the quality of the film can be diminished, thus leading to the need for further optimization. Regardless, the novelty of this work is the first of its kind. Because of this, the authors hope that these findings can act as a fundamental groundwork for similar works in future which study PEO deposition for non-valve CS materials.

Acknowledgments

The authors would like to thank the National Science Foundation (CHE-1429768) for allowing the use of the powder x-ray diffractometer. The authors would also like to acknowledge and thank the National Science Foundation (1852578) for providing financial support for this project.

Conflict of interest

The authors declare no conflict of interest.

References

1. A.M. Ralls, P. Kumar, and P.L. Menezes, Tribological Properties of Additive Manufactured Materials for Energy Applications: A Review, *Processes*, 2021, **9**(1), p 31.
2. A.M. Ralls, C. Flores, T. Kotowski, C. Lee, P. Kumar, and P.L. Menezes, 7 - Development of Surface Roughness from Additive Manufacturing Processing Parameters and Postprocessing Surface Modification Techniques, *Tribology of Additively Manufactured Materials*. P. Kumar, M. Misra, P.L. Menezes Ed., Elsevier, 2022, p 193–222.
3. A.M. Ralls, M. John, J. Noud, J. Lopez, K. LeSourd, I. Napier, N. Hallas, and P.L. Menezes, Tribological, Corrosion, and Mechanical Properties of Selective Laser Melted Steel, *Metals*, 2022, **12**(10), p 1732.
4. Y. Rao, Q. Wang, D. Oka, and C.S. Ramachandran, On the PEO Treatment of Cold Sprayed 7075 Aluminum Alloy and Its Effects on Mechanical, Corrosion and Dry Sliding Wear Performances Thereof, *Surf. Coat. Technol.*, 2020, **383**, 125271.
5. M. Ashokkumar, D. Thirumalaikumarasamy, T. Sonar, S. Deepak, P. Vignesh, and M. Anbarasu, An Overview of Cold Spray Coating in Additive Manufacturing, Component Repairing and Other Engineering Applications, *J. Mech. Behav. Mater.*, 2022, **31**(1), p 514–534.
6. A.M. Ralls, M. Daroonparvar, M. John, S. Sikdar, and P.L. Menezes, Solid-State Cold Spray Additive Manufacturing of Ni-Based Superalloys: Processing–Microstructure–Property Relationships, *Materials*, 2023, **16**(7), p 2765.
7. C.M. Sample, V.K. Champagne, A.T. Nardi, and D.A. Lados, Factors Governing Static Properties and Fatigue, Fatigue Crack Growth, and Fracture Mechanisms in Cold Spray Alloys and Coatings/Repairs: A Review, *Addit. Manuf.*, 2020, **36**, 101371.
8. W.-Y. Li and W. Gao, Some Aspects on 3D Numerical Modeling of High Velocity Impact of Particles in Cold Spraying by Explicit Finite Element Analysis, *Appl. Surf. Sci.*, 2009, **255**(18), p 7878–7892.
9. Y. Ichikawa, R. Tokoro, M. Tanno, and K. Ogawa, Elucidation of Cold-Spray Deposition Mechanism by Auger Electron Spectroscopic Evaluation of Bonding Interface Oxide Film, *Acta Mater.*, 2019, **164**, p 39–49.
10. M. Walker, Microstructure and Bonding Mechanisms in Cold Spray Coatings, *Mater. Sci. Technol.*, 2018, **34**(17), p 2057–2077.
11. H.M. Soltani and M. Tayebi, Comparative Study of AISI 304L to AISI 316L Stainless Steels Joints by TIG and Nd:YAG Laser Welding, *J. Alloys Compd.*, 2018, **767**, p 112–121.
12. H. Savaloni, E. Agha-Taheri, and F. Abdi, On the Corrosion Resistance of AISI 316L-Type Stainless Steel Coated with Manganese and Annealed with Flow of Oxygen, *J Theor Appl Phys*, 2016, **10**(2), p 149–156.
13. C.-O.A. Olsson and D. Landolt, Passive Films on Stainless Steels—Chemistry, Structure and Growth, *Electrochim. Acta*, 2003, **48**(9), p 1093–1104.
14. A.M. Ralls, M. Daroonparvar, A.K. Kasar, M. Misra, and P.L. Menezes, Influence of Friction Stir Processing on the Friction, Wear and Corrosion Mechanisms of Solid-State Additively Manufactured 316L Duplex Stainless Steel, *Tribol. Int.*, 2022, **66**, p 108033.
15. A.M. Ralls and P.L. Menezes, Understanding the Tribo-corrosion Mechanisms of Friction Stir Processed Steel Deposited by High-Pressure Deposition Additive Manufacturing Process, *Int. J. Adv. Manuf. Technol.*, 2023, **6**, p 66.
16. N.R. Baddoo, Stainless Steel in Construction: A Review of Research, Applications, Challenges and Opportunities, *J. Constr. Steel Res.*, 2008, **64**(11), p 1199–1206.
17. A. Hemmasian Ettefagh, S. Guo, and J. Raush, Corrosion Performance of Additively Manufactured Stainless Steel Parts: A Review, *Addit. Manuf.*, 2021, **37**, 101689.
18. W. Zhizhong, H. Chao, G. Huang, H. Bin, and H. Bin, Cold Spray Micro-Defects and Post-treatment Technologies: A Review, *Rapid Prototyp. J.*, 2021, **6**, p 66.
19. A.M. Ralls, M. Daroonparvar, S. Sikdar, M.H. Rahman, M. Monwar, K. Watson, C.M. Kay, and P.L. Menezes, Tribological and Corrosion Behavior of High Pressure Cold Sprayed Duplex 316 L Stainless Steel, *Tribol. Int.*, 2022, **169**, 107471.
20. T. Perard, A. Sova, H. Robe, V. Robin, Y. Zedan, P. Bocher, and E. Feulvarch, Friction Stir Processing of Austenitic Stainless Steel Cold Spray Coating Deposited on 304L Stainless Steel Substrate: Feasibility Study, *Int. J. Adv. Manuf. Technol.*, 2021, **115**(7), p 2379–2393.
21. S. Sikdar, P.V. Menezes, R. Maccione, T. Jacob, and P.L. Menezes, Plasma Electrolytic Oxidation (PEO) Process—Processing, Properties, and Applications, *Nanomaterials*, 2021, **11**(6), p 1375.
22. J. Martin, K. Akoda, V. Ntomprougkidis, O. Ferry, A. Maizeray, A. Bastien, P. Brenot and G. Ezo'o, and G. Henrion, Duplex Surface Treatment of Metallic Alloys Combining Cold-Spray and Plasma Electrolytic Oxidation Technologies, *Surf. Coat. Technol.*, 2020, **392**, 125756.
23. R. Chaharmahali, A. Fattah-Alhosseini and H. Esfahani, Increasing the In-Vitro Corrosion Resistance of AZ31B-Mg Alloy via Coating with Hydroxyapatite Using Plasma Electrolytic Oxidation, *J. Asian Ceram. Soc.*, 2020, **8**(1), p 39–49.
24. E. Matykina, A. Berkani, P. Skeldon, and G.E. Thompson, Real-Time Imaging of Coating Growth during Plasma Electrolytic Oxidation of Titanium, *Electrochim. Acta*, 2007, **53**(4), p 1987–1994.
25. K. Babaei, A. Fattah-alhosseini, and R. Chaharmahali, A Review on Plasma Electrolytic Oxidation (PEO) of Niobium: Mechanism, Properties and Applications, *Surf. Interfaces*, 2020, **21**, 100719.
26. A. Fattah-alhosseini, R. Chaharmahali, M.K. Keshavarz, and K. Babaei, Surface Characterization of Bioceramic Coatings on Zr and Its Alloys Using Plasma Electrolytic Oxidation (PEO): A Review, *Surf. Interfaces*, 2021, **25**, 101283.
27. A. Fattah-alhosseini, K. Babaei, and M. Molaei, Plasma Electrolytic Oxidation (PEO) Treatment of Zinc and Its Alloys: A Review, *Surf. Interfaces*, 2020, **18**, 100441.
28. E. Nikoomanzari, M. Karbasi, C.M.A. Melo, H. Moris, K. Babaei, S. Giannakis, and A. Fattah-alhosseini, Impressive Strides in Antibacterial Performance Amelioration of Ti-Based Implants via Plasma Electrolytic Oxidation (PEO): A Review of the Recent Advancements, *Chem. Eng. J.*, 2022, **441**, p 136003.
29. A. Fattah-alhosseini, R. Chaharmahali, and K. Babaei, Impressive Strides in Amelioration of Corrosion and Wear Behaviors of Mg Alloys Using Applied Polymer Coatings on PEO Porous Coatings: A Review, *J. Magn. Alloys*, 2022, **10**(5), p 1171–1190.
30. T. Zehra, A. Fattah-alhosseini, and M. Kaseem, Surface Properties of Plasma Electrolytic Oxidation Coating Modified by Polymeric Materials: A Review, *Prog. Org. Coat.*, 2022, **171**, 107053.
31. M. Karbasi, E. Nikoomanzari, R. Hosseini, H. Bahramian, R. Chaharmahali, S. Giannakis, M. Kaseem, and A. Fattah-alhosseini, A Review on Plasma Electrolytic Oxidation Coatings for Organic Pollutant Degradation: How to Prepare Them and What to Expect of Them?, *J. Environ. Chem. Eng.*, 2023, **11**(3), 110027.

32. G.-W. Lin, Y.-H. Huang, W. Tseng, and F.-H. Lu, Production of N-Doped Anatase TiO_2 on TiN-Coated Ti Substrates by Plasma Electrolytic Oxidation for Visible-Light Photocatalysts, *Ceram. Int.*, 2019, **45**(17), p 22506–22512.
33. Y. Zhang, Q. Wang, R. Ye, and C.S. Ramachandran, Plasma Electrolytic Oxidation of Cold Spray Kinetically Metallized CNT-Al Coating on AZ91-Mg Alloy: Evaluation of Mechanical and Surficial Characteristics, *J. Alloys Compd.*, 2022, **892**, 162094.
34. Y. Rao, Q. Wang, J. Chen, and C.S. Ramachandran, Abrasion, Sliding Wear, Corrosion, and Cavitation Erosion Characteristics of a Duplex Coating Formed on AZ31 Mg Alloy by Sequential Application of Cold Spray and Plasma Electrolytic Oxidation Techniques, *Mater. Today Commun.*, 2021, **26**, 101978.
35. N. Attarzadeh, M. Molaei, K. Babaei, and A. Fattah-alhosseini, New Promising Ceramic Coatings for Corrosion and Wear Protection of Steels: A Review, *Surf. Interfaces*, 2021, **23**, 100997.
36. X. Nie, R. Cai, C. Zhao, J. Sun, J. Zhang, and D.T.A. Matthews, Advancement of Plasma Electrolytic Oxidation towards Non-valve Metals, *Surf. Coat. Technol.*, 2022, **442**, 128403.
37. W. Yang, Q. Li, W. Liu, J. Liang, Z. Peng, and B. Liu, Characterization and Properties of Plasma Electrolytic Oxidation Coating on Low Carbon Steel Fabricated from Aluminate Electrolyte, *Vacuum*, 2017, **144**, p 207–216.
38. V.A. Andrei, C. Radulescu, V. Malinovschi, A. Marin, E. Coaca, M. Mihalache, C.N. Mihailescu, I.D. Dulama, S. Teodorescu, and I.A. Bucurica, Aluminum Oxide Ceramic Coatings on 316l Austenitic Steel Obtained by Plasma Electrolysis Oxidation Using a Pulsed Unipolar Power Supply, *Coatings*, 2020, **10**(4), p 318.
39. S.A. Karpushenkov, G.L. Shchukin, A.L. Belanovich, V.P. Savenko and A.I. Kulak, Plasma Electrolytic Ceramic-Like Aluminum Oxide Coatings on Iron, *J. Appl. Electrochem.*, 2010, **40**(2), p 365–374.
40. D. Nečas and P. Klapetek, Gwyddion: An Open-Source Software for SPM Data Analysis, *Centr. Eur. J. Phys.*, 2012, **10**(1), p 181–188.
41. *Standard Test Method for Conducting Potentiodynamic Polarization Resistance Measurements* [Online]. https://www.astm.org/g0059-97r20.html. Accessed: 04-Mar-2023.
42. *Electrochemical Corrosion Measurements-Galvanic Corrosion Gamry Instruments* [Online]. https://www.gamry.com/application-notes/corrosion-coatings/basics-of-electrochemical-corrosion-measurements/. Accessed: 28-Sep-2023.
43. A. Saikiran, S. Hariprasad, S. Arun, and N. Rameshbabu, Effect of Electrolyte Composition on Morphology and Corrosion Resistance of Plasma Electrolytic Oxidation Coatings on Aluminized Steel, *Surf. Coat. Technol.*, 2019, **372**, p 239–251.
44. P.V. Menezes, M.M. Elnagar, M. Al-Shakran, M.J. Eckl, P.W. Menezes, L.A. Kibler, and T. Jacob, In-Liquid Plasma for Surface Engineering of Cu Electrodes with Incorporated SiO_2 Nanoparticles: From Micro to Nano, *Adv. Func. Mater.*, 2022, **32**(6), p 2107058.
45. L. Zhu, R.S. Petrova, J.P. Gashinski, and Z. Yang, The Effect of Surface Roughness on PEO-Treated Ti-6Al-4V Alloy and Corrosion Resistance, *Surf. Coat. Technol.*, 2017, **325**, p 22–29.
46. P.L. Menezes, S.V. Kailas, and M.R. Lovell, Fundamentals of Engineering Surfaces, *Tribology for Scientists and Engineers: From Basics to Advanced Concepts*. P.L. Menezes, M. Nosonovsky, S.P. Ingole, S.V. Kailas, M.R. Lovell Ed., Springer, New York, 2013, p 3–41.
47. Z. Li, Y. Cheng, S. Kang, W. Tu, and Y. Cheng, A Re-understanding of the Breakdown Theory from the Study of the Plasma Electrolytic Oxidation of a Carbon Steel—A Non-Valve Metal, *Electrochim. Acta*, 2018, **284**, p 681–695.
48. L.O. Snizhko, A.L. Yerokhin, A. Pilkington, N.L. Gurevina, D.O. Misnyankin, A. Leyland, and A. Matthews, Anodic Processes in Plasma Electrolytic Oxidation of Aluminium in Alkaline Solutions, *Electrochim. Acta*, 2004, **49**(13), p 2085–2095.
49. W. Zhang, J.W. Elmer, and T. DebRoy, Kinetics of Ferrite to Austenite Transformation during Welding of 1005 Steel, *Scr. Mater.*, 2002, **46**(10), p 753–757.
50. S.-Z. Wang, J.-Y. Lyu, W. He, P.-J. Liu, and Q.-L. Yan, Thermal Decomposition and Combustion Behavior of Ion Conductive PEO-PAN Based Energetic Composites, *Combust. Flame*, 2021, **230**, 111421.
51. J.L. Xu, Q.F. Xiao, D.D. Mei, Y.X. Tong, Y.F. Zheng, L. Li, and Z.C. Zhong, Microstructure, Corrosion Resistance and Formation Mechanism of Alumina Micro-Arc Oxidation Coatings on Sintered NdFeB Permanent Magnets, *Surf. Coat. Technol.*, 2017, **309**, p 621–627.
52. A.M. Ralls, A.K. Kasar, and P.L. Menezes, Friction Stir Processing on the Tribological, Corrosion, and Erosion Properties of Steel: A Review, *J. Manuf. Mater. Process.*, 2021, **5**(3), p 97.
53. *ImageJ* [Online]. https://imagej.net/ij/index.html. Accessed: 18-Aug-2023.
54. T. Hong and M. Nagumo, Effect of Surface Roughness on Early Stages of Pitting Corrosion of Type 301 Stainless Steel, *Corros. Sci.*, 1997, **39**(9), p 1665–1672.
55. M. Daroonparvar, M.U.F. Khan, Y. Saadeh, C.M. Kay, A.K. Kasar, P. Kumar, L. Esteves, M. Misra, P. Menezes, P.R. Kalvala, H.R. Bakhsheshi-Rad, and R.K. Gupta, Modification of Surface Hardness, Wear Resistance and Corrosion Resistance of Cold Spray Al Coated AZ31B Mg Alloy Using Cold Spray Double Layered Ta/Ti Coating in 3.5 wt% NaCl Solution, *Corros. Sci.*, 2020, **176**, 109029.
56. L. Pezzato, K. Brunelli, P. Dolcet, and M. Dabalà, Plasma Electrolytic Oxidation Coating Produced on 39NiCrMo3 Steel, *Surf. Coat. Technol.*, 2016, **307**, p 73–80.
57. J. Nie, L. Wei, Y. Jiang, Q. Li, and H. Luo, Corrosion Mechanism of Additively Manufactured 316 L Stainless Steel in 3.5 wt.% NaCl Solution, *Mater. Today Commun.*, 2021, **26**, p 101648.
58. M. Daroonparvar, A. Helmer, A.M. Ralls, A.K. Kasar, M.U. Farooq Khan, P.L. Menezes, M. Misra, S. Shao, and R.K. Gupta, Study on the Corrosion Behavior of Cold Sprayed Aluminum-Based Coatings on Mg-Based Alloy in Chloride Containing Solution: Effect of N2 Processing Gas Temperature, *Corros. Sci.*, 2023, **223**, 111454.
59. V.A. Andrei, E. Coaca, M. Mihalache, V. Malinovschi, and M. Patrascu-Minca, Study of Ceramic-Like Aluminum Oxide Thin Films Developed Using Plasma Electrolytic Oxidation Applied on Austenitic Steels, *Surf. Interface Anal.*, 2016, **48**(7), p 654–659.
60. E. Coacă, O.A. Rusu, A.H. Marin, M. Mihalache, V.A. Andrei, and T. Vişan, "*Microscopic And Electrochemical Characterization Of Alumina Ceramic Films Developed Onto 316l Stainless Steel By Micro-Arc Oxidation In Plasma Electrolysis*".
61. A.C. Hall, L.N. Brewer, and T.J. Roemer, Preparation of Aluminum Coatings Containing Homogenous Nanocrystalline Microstructures Using the Cold Spray Process, *J. Therm. Spray Technol.*, 2008, **17**(3), p 352–359.
62. J.A. Curran and T.W. Clyne, The Thermal Conductivity of Plasma Electrolytic Oxide Coatings on Aluminium and Magnesium, *Surf. Coat. Technol.*, 2005, **199**(2), p 177–183.
63. H. Dong, B. Wen, and R. Melnik, Relative Importance of Grain Boundaries and Size Effects in Thermal Conductivity of Nanocrystalline Materials, *Sci. Rep.*, 2014, **4**(1), p 7037.
64. X. Shen, X. Nie, H. Hu, and J. Tjong, Effects of Coating Thickness on Thermal Conductivities of Alumina Coatings and Alumina/Aluminum Hybrid Materials Prepared Using Plasma Electrolytic Oxidation, *Surf. Coat. Technol.*, 2012, **207**, p 96–101.
65. G. Altuntaş, O. Altuntaş, M.K. Öztürk, and B. Bostan, Metallurgical and Crystallographic Analysis of Different Amounts of Deformation Applied to Hadfield Steel, *Int. Metalcast.*, 2022, **6**, p 66.
66. S. Rahimi, T.N. Konkova, I. Violatos, and T.N. Baker, Evolution of Microstructure and Crystallographic Texture during Dissimilar Friction Stir Welding of Duplex Stainless Steel to Low Carbon-Manganese Structural Steel, *Metall. Mater. Trans. A*, 2019, **50**(2), p 664–687.
67. B. Yoo, K.R. Shin, D.Y. Hwang, D.H. Lee, and D.H. Shin, Effect of Surface Roughness on Leakage Current and Corrosion Resistance of Oxide Layer on AZ91 Mg Alloy Prepared by Plasma Electrolytic Oxidation, *Appl. Surf. Sci.*, 2010, **256**(22), p 6667–6672.
68. B. Díaz, E. Härkönen, V. Maurice, J. Światowska, A. Seyeux, M. Ritala, and P. Marcus, Failure Mechanism of Thin Al2O3 Coatings Grown by Atomic Layer Deposition for Corrosion Protection of Carbon Steel, *Electrochim. Acta*, 2011, **56**(26), p 9609–9618.
69. K. Leung, First Principles, Explicit Interface Studies of Oxygen Vacancy and Chloride in Alumina Films for Corrosion Applications, *J. Electrochem. Soc.*, 2021, **168**(3), 031511.